Chemical Engineering Journal Advances 27 (2026) 101283

Contents lists available at ScienceDirect

Chemical Engineering Journal Advances

journal homepage: www.sciencedirect.com/journal/chemical-engineering-journal-advances

Process-informed optimal design principles for cooperative step-isotherm adsorbents in direct air capture using ANN-accelerated TVSA modelling

Maryam Nasiri Ghiri [a], Hamid Reza Nasriani [a,*], Mohammad Bagheri [b], Leila Khajenoori [a], Samira khani Rasmussen [c], Andrei Chamchine [a]

[a] School of Engineering & Computing, University of Lancashire, Preston PR1 2HE, UK
[b] School of Chemical Engineering, University of Tehran, Iran
[c] Geological Survey of Denmark and Greenland, Department of Geo-Energy and Storage, ΦsterVoldgade 10, 1350 Copenhagen, Denmark

ARTICLE INFO

Keywords:
Direct air capture
Cooperative adsorption
Step-shaped isotherms
Temperature–vacuum swing adsorption
Process-informed adsorbent design
Adsorption
Metal–organic frameworks

ABSTRACT

Direct air capture (DAC) using solid sorbents is limited by energy demand and productivity, which depend strongly on adsorbent properties. Cooperative adsorbents with step-shaped isotherms are promising for capturing CO_2 from ultra-dilute air, but the link between isotherm characteristics and process performance remains unclear. This work couples a validated packed-bed temperature–vacuum swing adsorption (TVSA) model with an artificial neural network (ANN) surrogate to explore the multi-dimensional design space of cooperative sorbents, using mmen–Mg_2(dobpdc) as a benchmark. The surrogate model is trained on 2866 simulation data points to enable efficient sensitivity analysis and optimisation.

Results reveal a clear hierarchy of control: step pressure (P_{step0}), step enthalpy (ΔH_{step}), and high-loading enthalpy (ΔH_{High}) dominate specific energy consumption (SEC), productivity, and purity, whereas kinetics show minor influence under the studied regime. Significant second-order interactions were identified between P_{step0} and ΔH_{step}, highlighting the coupled role of step position and energetics. Surrogate-assisted design exploration identifies an optimal design region, characterised by low step pressure, moderate step enthalpy, and high adsorption capacity. A representative optimal isotherm improves CO_2 recovery from 53% to 76% and increases productivity by approximately 38%, while reducing energy consumption to 2.9 MJ/kg CO_2 at ~98% purity. These improvements arise from aligning the adsorption step with the DAC operating window while maintaining favourable adsorption energetics. Importantly, these findings establish process-informed design principles, enabling targeted tuning of material properties for improved DAC performance.

1. Introduction

To meet net-zero targets and mitigate the impact of climate change, a multifaceted energy transition is required. Effective carbon mitigation necessitates a multidisciplinary framework that bridges the gap between clean energy production and robust atmospheric removal. Green energy production approaches, such as sustainable hydrogen generation and advances in CO_2 sequestration could make direct air capture more impactful by providing scalable and efficient permanent storage solutions [1,2]. Within the suite of carbon capture technologies, adsorption-based separation processes have emerged as a promising solution due to their scalability, energy efficiency, and the ability to operate under a wide range of conditions [3–5]. The effectiveness of these systems is strongly dictated by the properties of the solid sorbent, which determine the capture capacity, selectivity, and the energy requirements for regeneration. Sorbent performance is influenced not only by physical attributes, such as surface area, pore structure, particle size, etc., but also by the adsorption isotherm parameters, including capacity, affinity, shape parameters, etc. [6,7]. A systematic investigation of these variables is essential to get a better understanding of their influence on adsorption behaviour and process performance. To this end, extensive research has focused on different modification strategies aimed at improving the porosity, surface area, adsorption capacity and selectivity [8].

Broadly, these modification strategies are categorised into defect engineering and functionalisation approaches. Defect engineering utilises structural imperfections in the framework to create more porosity or generate additional active sites [9,10]. The influence of pore geometry, structural defectivity, and solvent coordination on the adsorption characteristics of Mg_2(dobpdc) has been extensively characterised using

---

* Corresponding author at: University of Lancashire, United Kingdom of Great Britain and Northern Ireland.
E-mail address: HRNasriani@lancashire.ac.uk (H.R. Nasriani).

https://doi.org/10.1016/j.ceja.2026.101283

Nomenclature

PIs	Performance indicators
ΔH_{High}	Adsorption enthalpy in the high-loading regime beyond the step
ΔH_{CO2}	CO_2 heat of adsorption (kJ mol^{-1})
P_{step0}	Characteristic step pressure
n_A	Kinetic Avrami exponent
q_H	Maximum CO_2 uptake
n_0	Cooperative adsorption at low coverage
R_2	Coefficient of determination
AARD	Average absolute relative deviation
RMSE	Root mean squared error
LHS	Latin Hypercube Sampling
Var (Y)	Total variance of the model output
f(A)j	Model output of the jth sample of the A matrix
f(B)j	Model output of the jth sample of the B matrix
$f\left(A_B^i\right)_j$	Model output obtained by replacing the ith column of B with that of A
Y	Output variable (SEC, purity, recovery, or productivity)
$Y_{predicted}$	Predicted value by ANN
Y_{actual}	Actual value of performance indicators
VSA	Vacuum swing adsorption
ΔH_{step}	Enthalpy associated with the cooperative adsorption step
GA	Genetic algorithm

Abbreviation

PEI	Polyethyleneimine
FTIR	Fourier Transform Infrared Spectroscopy
ANN	Artificial Neural Network
SEC	Specific energy consumption (MJ/Kg CO_2)
DAC	Direct Air Capture
MOF	Metal Organic Framework
CCUS	Carbon capture, utilisation, and storage
TVSA	Temperature vacuum swing adsorption
TEPA	Tetraethylenepentamine
LDF	Linear driving force
S-TVSA	Steam assistance TVSA
PVSA	Pressure vacuum swing adsorption
TSA	Temperature Swing Adsorption

IR spectroscopy and quantum calculations. Research indicates that the open metal site availability and solvent binding exert a great effect on the adsorption energetics. Furthermore, while certain metal-organic frameworks (MOFs) may experience severe structural collapse under humid conditions, exemplified by an 83% loss in surface area, FTIR measurements have demonstrated that sorption behaviour can remain largely unaffected. This observation highlights both the intrinsic resilience of the material's active sites and the inherent challenges in detecting structural degradation through spectroscopic techniques alone [11].

Functionalisation approaches, by contrast, introduce specific chemical moieties into the framework to promote stronger and more selective interactions with target molecules. In metal organic frameworks (MOFs), this is usually achieved by the grafting of amine groups in open metal sites, or on organic linkers, providing chemisorptive binding by the formation of carbamate or carbamic acid species [12,13]. The Mg_2(dobpdc) framework, which has been widely studied for CO_2 capture, has been investigated under both defect engineering to modify its structure, as well as amine functionalisation to introduce chemically reactive sites [14]. The CO_2 adsorption behaviour of diamine-appended Mg_2(dobpdc) frameworks is governed by the cooperative insertion of CO_2 into metal–amine bonds, which produces a characteristic step-shaped isotherm. The pressure at which this adsorption step occurs is highly sensitive to the properties of the metal sites, the structure and dynamics of the appended diamines, and the operating temperature [12, 14]. Even small variations in amine structure or loading that shift the step pressure can have a pronounced effect on adsorption efficiency, product purity, and energy consumption [15,14]. Consistent with this sensitivity, Siegelman et al. [16] demonstrated that modifying the diamine structure across nine variants shifts the pressure at the adsorption step by more than four orders of magnitude at a fixed temperature, highlighting the exceptional tunability of CO_2 adsorption in these frameworks. Other studies have systematically compared amines with different molecular sizes, such as N,N′-dimethylethylenediamine (m-2-m), tetraethylenepentamine (TEPA), and polyethyleneimine (PEI). Results suggested that both types of amine and operating conditions have a strong impact on the adsorption performance: the enhanced CO_2 adsorption capacity of TEPA-impregnated Mg_2(dobpdc) under humid conditions, due to decreased diffusion limitations, was observed, whereas the materials functionalised with PEI were morphologically degraded during cycling [17].

Given the staggering complexity and almost unlimited combinations of these modular building blocks (around 100,000 MOFs), to fully explore this potential and to identify optimal candidates for specific gas adsorption applications, numerous studies have employed machine learning (ML) to screen vast databases, such as CoRE, h-MOF, and MOFomics [18–21]. While these studies effectively correlate geometric descriptors and metal-centre chemistry with static adsorption capacity, their practical impact is often constrained by the assumption that basic metrics such as Henry selectivity or CO_2 capacity are sufficient indicators of process-level success. This narrow focus creates a critical gap: the tremendous potential of MOFs exerts significant pressure on traditional process development, yet identifying a promising material in a database does not guarantee efficient performance in a dynamic industrial cycle. Consequently, moving beyond material-centric screening to a process-aware evaluation is essential for realising the true potential of these adsorbents. To address this, Luukkonen and Elfving used global sensitivity analysis and dynamic TVSA/S-TVSA simulations to identify key parameters controlling DAC performance and cost, providing guidance for adsorbent design under atmospheric CO_2 conditions [22]. Although such simulation-based approaches reduce the need for expensive and time-consuming experimental procedures, the computational intensity remains high, especially when multiple parameters are varied, as each simulation requires solving complex sets of partial differential equations over multiple cycles to reach a cyclic steady state. Consequently, shortcut models have been proposed to bridge the gap between simplified metrics, such as isotherm inspection or selectivity, and the computationally intensive full-scale simulations [23–25].

A shortcut pressure vacuum swing adsorption (PVSA) model revealed that adsorbent selectivity and thermal effects had a significant impact on specific power consumption than CO_2 capacity, with an optimal CO_2 heat of adsorption in the range of 35–45 kJ mol^{-1}. Moreover, high surface area can be detrimental, as increased porosity may promote N_2 co-adsorption and reduce overall selectivity [24]. Similarly, shortcut models for temperature swing adsorption (TSA) processes offer a computationally efficient framework for the rapid screening of CO_2 capture performance from flue gas by assuming local equilibrium and simplified kinetics to predict cyclic steady state performance efficiency [23]. However, shortcut models are often inadequate for amine-functionalised sorbents due to their slow adsorption kinetics. As corroborated by Danaci et al. [26], while these models suit equilibrium-driven materials like zeolites and activated carbons, they failed for kinetically hindered systems. By assuming instantaneous equilibrium, shortcut models overlook critical mass and heat transfer phenomena, leading to substantial errors that only detailed dynamic models can accurately resolve. Consequently, adsorbents characterised by slow cooperative kinetics are more accurately evaluated using detailed, rate-based process simulations rather than equilibrium-based shortcut methods [23,27].

To overcome the prohibitive computational cost of rate-based dynamic simulations, Machine Learning (ML) models can be implemented as efficient surrogates. By training on a representative dataset generated from experimentally validated detailed process simulations, ML models bypass intensive numerical integrations, enabling rapid system performance predictions across extensive parameter spaces. Specifically, surrogate-assisted frameworks have been successfully employed to optimise Vacuum Pressure Swing Adsorption (VPSA) systems using flexible MOFs with complex sigmoidal isotherms, significantly reducing the computational burden of navigating hysteretic performance maps [28]. Furthermore, similar ML-based approaches have been utilised for the cyclic performance optimisation of DAC using amine-functionalized MOFs, demonstrating that surrogate models can improve process configurations with minimal time requirements compared to traditional physics-based solvers [27]. The data-driven approach facilitates robust global sensitivity analysis (GSA), capturing the complex, nonlinear interactions between isotherm and sorbent parameters that remain computationally inaccessible via detailed simulation alone [29]. These models not only offer high-throughput screening capabilities but also facilitate the exploration of structure-performance relationships that can inform mechanistic hypotheses regarding process-level behaviour and guide rational material design. For example, this framework was successfully applied to Lewatit VP OC 1065 under TVSA and S-TVSA conditions; the ANN-based GSA accurately quantified the relative importance of varying adsorbent and process parameters on key performance indicators (KPIs), elucidating their individual and synergetic impacts on adsorption efficiency [29]. A similar data-driven approach was employed to optimise plastic-derived porous carbons, using ML to reveal the structural features governing CO_2 capture. By employing ANN surrogate models to scale technical routes via process simulations, the study achieved high exergy efficiency and provided systematic guidelines for the development of sustainable, high-performance adsorbents [30]. This integrated approach was recently exemplified by the PrISMa platform [31,32], which leverages an ML feedback loop to link molecular crystal structures directly to techno-economic and life-cycle assessments across thousands of case studies. By identifying chemically diverse clusters of top-performing materials for specific source-sink pairs, such platforms demonstrate that ML is essential for bridging the gap between material design and industrial-scale deployment.

While recent integrated platforms have pioneered the simultaneous evaluation of materials and techno-economics at scale [29], a critical gap remains in the high-fidelity optimisation of non-ideal cooperative adsorbents. These materials demonstrate exceptional potential for DAC due to their unique step-shaped behaviour, yet most process-informed screenings rely on conventional Langmuir-type representations that fail to capture this complexity. To fully realise the advantages of cooperative adsorbents, it is essential to move beyond broad screening toward a detailed analysis of how molecular-level isotherm properties interact with dynamic process variables. This work bridges the gap between molecular-level tuning and system performance by establishing a quantitative property-performance nexus. While traditional studies

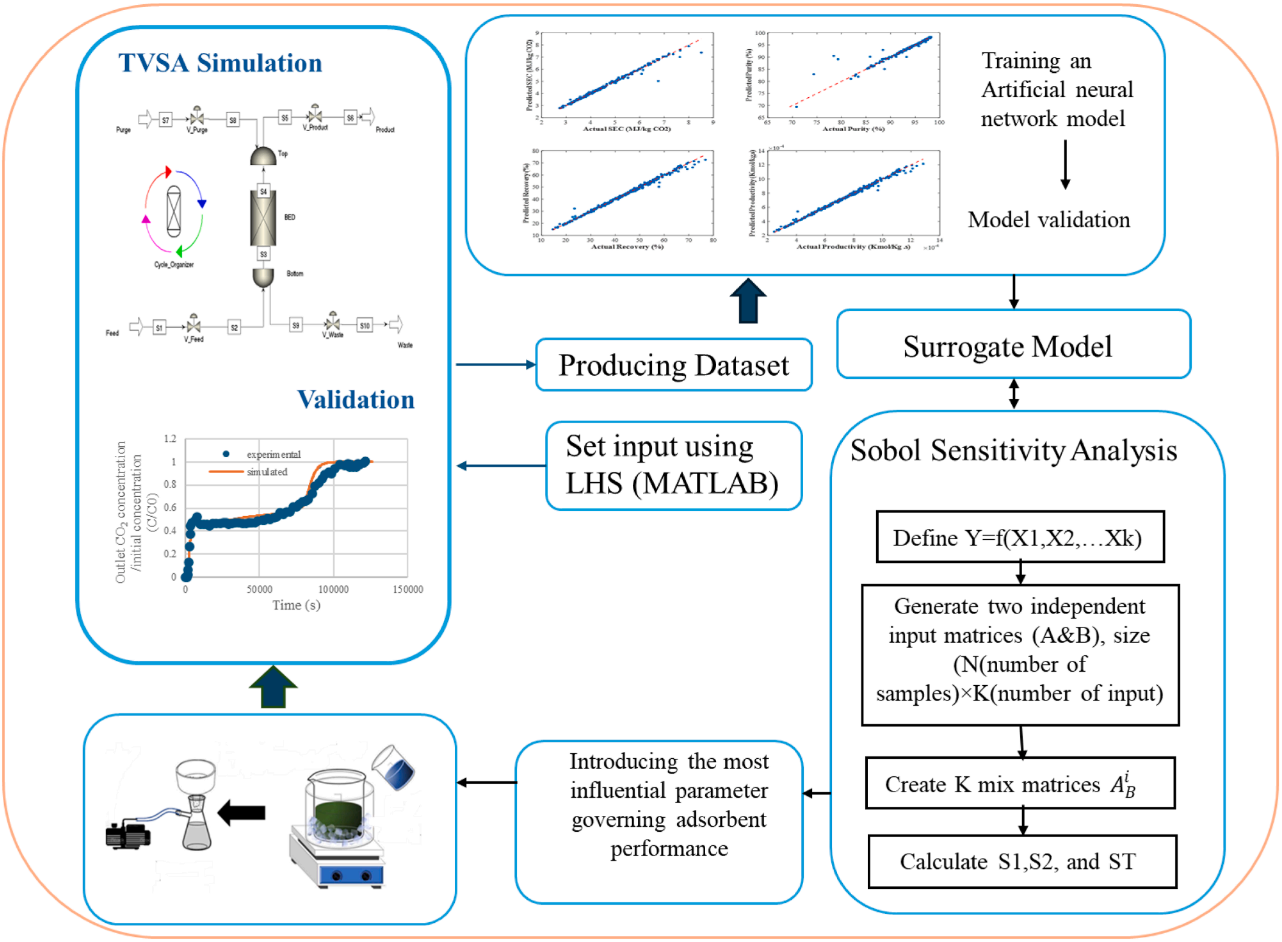

Fig. 1. Schematic representation of the integrated methodology used in this study, combining process simulation, ANN surrogate modelling, and Sobol global sensitivity analysis.

evaluate adsorbents based on static metrics (e.g., capacity or selectivity), our integrated framework translates these molecular descriptors into dynamic process indicators (SEC, productivity, and purity). By defining the numerical design windows for cooperative sorbents, we provide a prescriptive roadmap for synthetic chemists to optimise material tunability in a way that is directly informed by the constraints of a full TVSA cycle.

An overview of the integrated methodology and its role in linking molecular descriptors to system-level performance is provided in Fig. 1.

2. Methodology

2.1. Model description of the TVSA process

To evaluate the performance of mmen-Mg_2(dobpdc) under DAC conditions, a dynamic TVSA model was developed using Aspen Adsorption V14. The model simulates the complete adsorption/desorption cycle by solving the coupled mass, energy, and momentum balances and quantifying key process performance indicators, including CO_2 purity, recovery, productivity, and specific energy consumption (SEC). The TVSA cycle consists of five sequential steps: adsorption, evacuation, heating, cooling, and pressurisation. The operating conditions and cycle parameters used in this study are summarised in Table 1, and the value of adsorbent and bed specification are shown in Table S1.

The governing equations, kinetics, equilibrium formulations, and model parameters are comprehensively described in our previous work [33]. The process model assumes a one-dimensional packed bed, with radial variations neglected and both the adsorbent and wall properties are considered uniform. The gas phase is treated as an ideal mixture, a reasonable approximation given the low operating pressures and dilute CO_2 concentrations typical of DAC systems. Adsorption is modelled as a non-isothermal, adiabatic process to ensure a comprehensive capture of the system's thermal-kinetic coupling. This approach is validated by the reference study [34], which provided the experimental basis for our simulations. Their sensitivity analysis (Figures S7–S9 of this study) demonstrates that at ultra-dilute feed concentrations (400 ppm), the temperature rise in an adiabatic bed is negligible, resulting in nearly identical breakthrough to those observed under isothermal conditions. By adopting the adiabatic framework, the model maintains high physical fidelity and remains consistent with the experimental results while accounting for the potential impact of heat of adsorption during the breakthrough process. The heat of adsorption and specific heat capacities are assumed constant because the amount of adsorbed CO_2 is small in DAC, while the pressure drop along the column is evaluated using the Ergun correlation. Adsorption kinetics are captured through a hybrid formulation: below the step pressure, the linear driving force (LDF) model is employed to describe macropore diffusion resistance, whereas above the step pressure, the Avrami fractional-order model is applied to represent the nucleation-and-growth mechanism characteristic of cooperative adsorption. The equilibrium adsorption behaviour is described using the Sip isotherm model introduced by Darunte et al. [34], which captures the step-shaped cooperative adsorption characteristic of diamine-functionalised frameworks. The accuracy of this modelling framework and its underlying assumptions has been rigorously validated against experimental data in a previous study, demonstrating close agreement across a range of operating conditions [33]. As illustrated in Fig. 2, the model demonstrates close agreement with experimental results [34] across a diverse range of operating conditions, confirming its reliability for this study.

Table 1
Process parameters and cycle durations for the base case.

Process Parameters	Unit	Values
Adsorption Time	s	7200
Evacuation Time	s	6
Heating+ Evacuation Time	s	1000
Cooling Time	s	Temperature matched the feed temperature
Pressurising Time	s	Pressure matched the atmospheric pressure
Feed Flow rate	Kmol/hr	3e-4
Feed Temperature	°C	23
Desorption Temperature	°C	120
Evacuation Pressure	bar	0.09

Given that this study focuses on the influence of isotherm parameters, the corresponding isotherm equation, fitted parameters, and temperature-dependent relationships are shown in Fig. 2. This validated TVSA model subsequently served as the high-fidelity foundation for generating the comprehensive dataset required to train and validate the machine-learning surrogate models. In this study, to isolate the effect of adsorbent properties, the process configuration was fixed according to the baseline conditions reported in [33], as summarised in Table 1.

2.2. Parameter identification and physical significance

To investigate the relationship between adsorbent parameters and their influence on process performance, specifically CO_2 purity, recovery, productivity, and SEC, calculated according to the formulations in [33], the variables of interest and their corresponding tunable ranges were first identified. This selection encompasses fundamental adsorbent properties, primarily focusing on thermodynamic parameters, which consist of isotherm descriptors and the heat of adsorption, alongside adsorption kinetics. Due to the high dimensionality of the cooperative isotherm model, a preliminary screening was conducted to categorise the variables based on their influence on specific isotherm regions: the low-pressure (initial uptake), transition (step-wise), and high-pressure (saturation) regions. For each category, the most representative parameter was selected to reduce the input space for the surrogate model.

The low-pressure region, corresponding to the initial portion of the isotherm prior to the step-change, is characterised by CO_2 molecules not yet overcoming the energy barrier for cooperative insertion. This region is mainly governed by the isotherm parameters such as n_0, ΔH_n, ΔH_L, b_{L0}, P_{step0}, ΔH_{step} and q_L as summarised in Table 2. The pronounced low-pressure region is disadvantageous in practical application because it leads to lower bed utilisation and CO_2 loss. Fig. 3a and h illustrated n_0 (the cooperative adsorption at low coverage) and P_{step0} (the characteristic step pressure) exert the largest impact on the low-pressure region. Therefore, they are considered representative descriptors of this part of the isotherm.

The parameters b_{L0}, λ_1, ΔH_{High}, and ΔH_{step}, P_{step0} primarily govern the transition region of the isotherm (Table 2). A sharper breakthrough corresponds to a narrower transition region, indicating more efficient bed utilisation, while a broader transition region results in more gradual uptake, early CO_2 breakthrough, and reduced utilisation of the adsorbent [34]. To investigate how variations in the transition region influence breakthrough behaviour and process performance, the adsorption enthalpy at high loading (ΔH_{High}) and the cooperative adsorption step (ΔH_{step}) were selected for detailed sensitivity analysis, as these parameters most directly control the steepness of the adsorption step (Fig. 3e and g).

The final part of the isotherm, known as the high-pressure (saturation) region, is characterised by the parameters q_H, q_{u0}, and ΔH_u (Table 2). The parameter q_H defines the maximum adsorption capacity in the high-loading regime, representing the plateau that follows the sharp uptake step in the cooperative isotherm model. Physically, q_H corresponds to the total density of available adsorption sites activated through the cooperative interactions. Unlike q_{u0} and ΔH_u, which mainly affect the upper end of the plateau, Fig. 3l shows, q_H, uniformly shifts the entire saturation region upward or downward. This parameter has a direct effect on the working capacity and bed utilisation, independent of

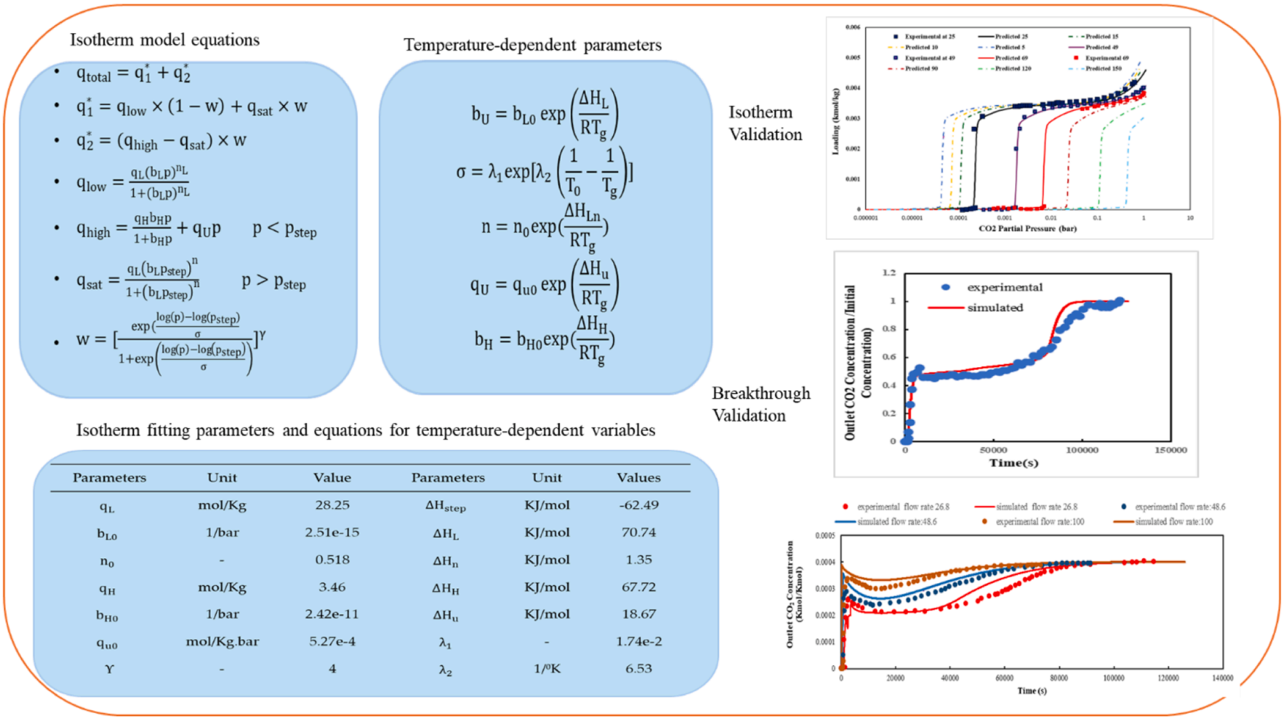

Isotherm model equations

- $q_{total} = q_1^* + q_2^*$
- $q_1^* = q_{low} \times (1 - w) + q_{sat} \times w$
- $q_2^* = (q_{high} - q_{sat}) \times w$
- $q_{low} = \frac{q_L (b_L p)^{n_L}}{1 + (b_L p)^{n_L}}$
- $q_{high} = \frac{q_H b_H p}{1 + b_H p} + q_U p \qquad p < p_{step}$
- $q_{sat} = \frac{q_L (b_L p_{step})^n}{1 + (b_L p_{step})^n} \qquad p > p_{step}$
- $w = [\frac{\exp(\frac{\log(p) - \log(p_{step})}{\sigma})}{1 + \exp\left(\frac{\log(p) - \log(p_{step})}{\sigma}\right)}]^{\gamma}$

Temperature-dependent parameters

$$b_U = b_{L0} \exp\left(\frac{\Delta H_L}{RT_g}\right)$$

$$\sigma = \lambda_1 \exp[\lambda_2 \left(\frac{1}{T_0} - \frac{1}{T_g}\right)]$$

$$n = n_0 \exp(\frac{\Delta H_{Ln}}{RT_g})$$

$$q_U = q_{u0} \exp\left(\frac{\Delta H_u}{RT_g}\right)$$

$$b_H = b_{H0} \exp(\frac{\Delta H_H}{RT_g})$$

Isotherm fitting parameters and equations for temperature-dependent variables

Parameters	Unit	Value	Parameters	Unit	Values
q_L	mol/Kg	28.25	ΔH_{step}	KJ/mol	-62.49
b_{L0}	1/bar	2.51e-15	ΔH_L	KJ/mol	70.74
n_0	-	0.518	ΔH_n	KJ/mol	1.35
q_H	mol/Kg	3.46	ΔH_H	KJ/mol	67.72
b_{H0}	1/bar	2.42e-11	ΔH_u	KJ/mol	18.67
q_{u0}	mol/Kg.bar	5.27e-4	λ_1	-	1.74e-2
Υ	-	4	λ_2	1/°K	6.53

Fig. 2. The isotherm equation, fitted parameters, and temperature-dependent relationships of the Sips isotherm model developed by [34].

Table 2
Classification of isotherm parameters according to their influence on different regions of the adsorption isotherm.

Low-pressure region	Transition region	High Pressure (Saturation) Region
n_0	b_{H0}	q_H
q_L	λ_1	q_{U0}
b_{L0}	ΔH_{High}	ΔH_U
P_{step0}	ΔH_{step}	
ΔH_{step}	P_{step0}	
ΔH_{Low}		
ΔH_n		

step position or low-pressure region. The incorporation of q_H in the sensitivity analysis consequently allows a systematic consideration of the effect of variation in the ultimate adsorption capacity on the process performance.

To understand the role of the heat of adsorption, the enthalpy of CO_2 adsorption (ΔH_{CO2}) is also included in the sensitivity analysis. This parameter governs the thermal effects associated with adsorption and desorption, directly impacting regeneration energy requirements and separation performance. Additionally, as demonstrated by Siegelman et al. [16], the position of the cooperative adsorption step is influenced by the CO_2 adsorption enthalpy through its contribution to the adsorption free energy, which in turn affects the overall effectiveness of cooperative adsorbents. Incorporation of ΔH_{CO2} thus enables a detailed investigation into how changes in heat of adsorption impact both the thermal efficiency and operational limits of the DAC process.

In addition to thermodynamic parameters, one further parameter was considered in the sensitivity analysis, the Avrami exponent (n_A), which characterises the adsorption kinetics. The adsorption rate is described using the differential form of the Avrami model (Eq. (1)) [34]:

$$\frac{\partial W_i}{\partial t} = k_A^{n_A} t^{n_A - 1} (w^*{}_i - w_i) \tag{1}$$

where k_A is the Avrami rate constant, n_A is the Avrami fractional exponent, t is time, and $w^*{}_i$ is the equilibrium loading. The constant parameters (K_A) and (n_A) were fitted to experimental data, with representative values of $k_A = 4.36e\text{-}5$ (1/s) and $n_A = 1.5$ for 0.4 mbar CO_2 partial pressure and 23 °C, consistent with established literature values for cooperative chemisorption systems [34].

Physically, the overall rate of nucleation and growth process is controlled by k_A, while the mechanistic pathway and effective dimensionality of growth are characterised by n_A, which significantly influence the duration of the induction period [35]. In such materials, n_A governs how rapidly adsorption accelerates once nucleation occurs, thereby influencing the duration of the initial low-uptake regime before the step transition. Unlike the isotherm parameters, which determine equilibrium capacity and step position, n_A primarily affects the shape and progression of the adsorption curve rather than simply scaling the overall rate. Consequently, n_A was selected as the kinetic parameter in the sensitivity analysis, as variations in this parameter can meaningfully influence breakthrough, bed utilisation, and other key process performance indicators under the investigated operating conditions. Ultimately, seven representative parameters, n_A, ΔH_{CO2}, q_H, ΔH_{High}, ΔH_{step}, P_{step0}, and n_0 were selected as the model input vector. This selection enables a systematic investigation into the relationships between fundamental material property variations and the resulting process performance outputs.

2.3. Definition of parameter ranges and boundary justification

A model-driven, single-variable sensitivity analysis approach was used to define the acceptable ranges for four isotherm parameters: ΔH_{High}, ΔH_{step}, q_H, and n_0. The preliminary analysis ensured that variation in these parameters induced meaningful modifications in the adsorption behaviour while maintaining physically realistic isotherm shapes. The outcome of this analysis is illustrated in Fig. 4, and the corresponding parameter ranges are summarised in Table 3. The remaining properties, the n_A, ΔH_{CO2}, and P_{step0}, were assigned bounds based on literature data. These selected intervals show representative tunable ranges for diamine-appended Mg_2(dobpdc) variants, spanning the broad chemical tunability reported in experimental studies. For instance, a slight structural modification of the diamine ligands can shift

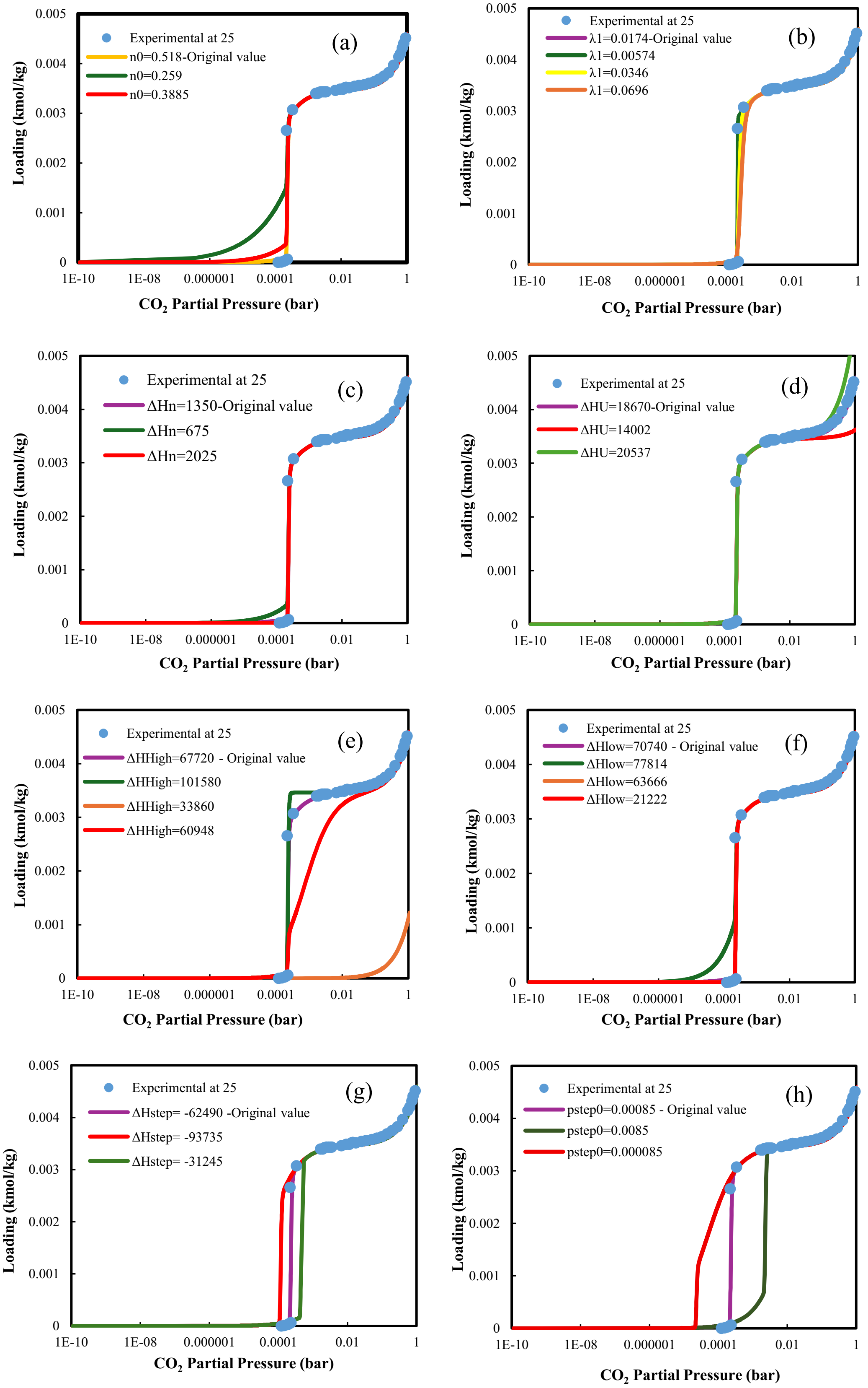

Fig. 3. Effect of isotherm parameters on the shape of the CO_2 adsorption isotherm for mmen–Mg_2(dobpdc); symbols represent experimental data at 25 °C [34].

the adsorption step pressure by more than four orders of magnitude at a fixed temperature [16,36]. This remarkable tunability highlights the

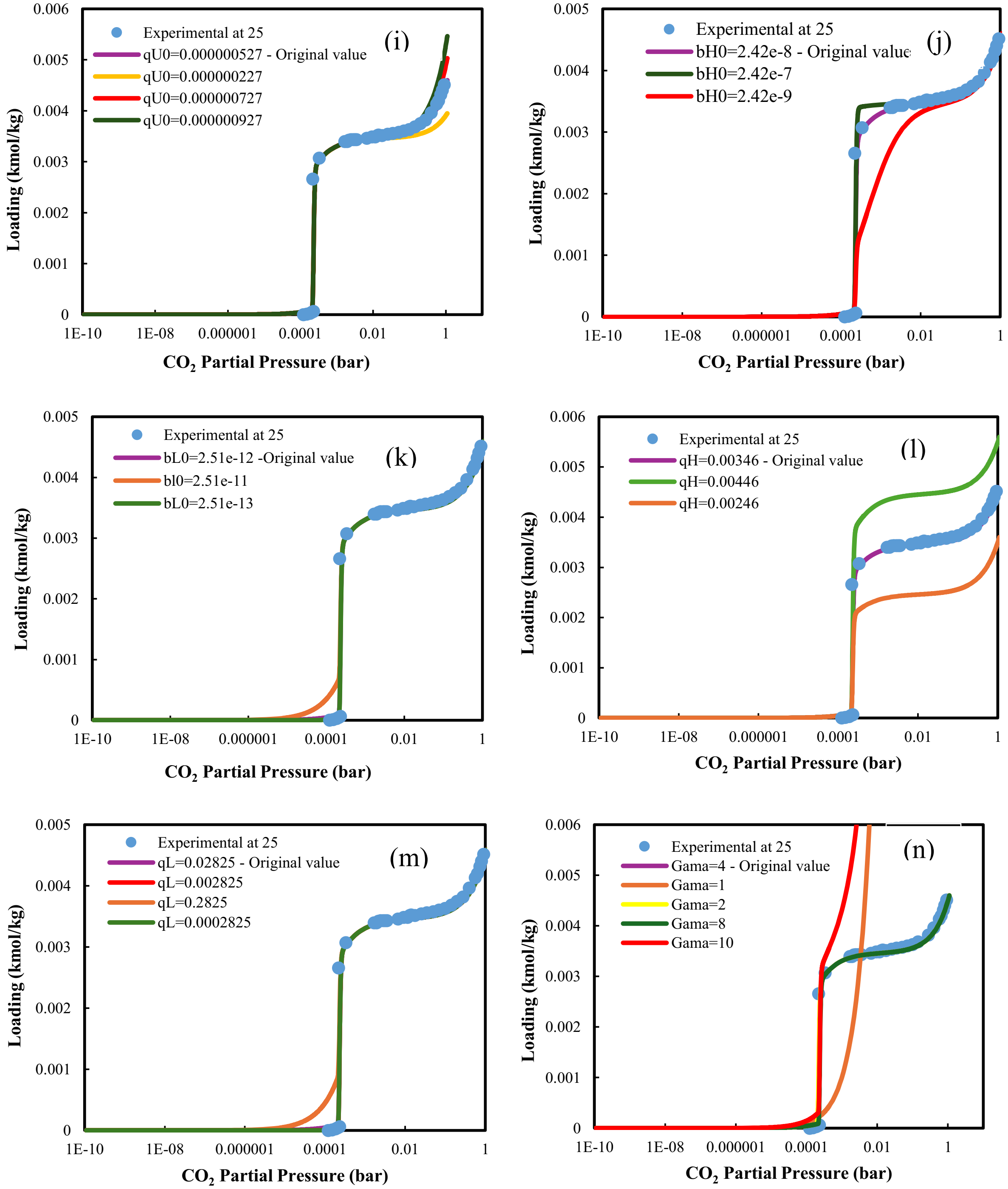

Fig. 3. (*continued*).

strong dependence of step location on molecular-level interactions and justifies the exploration of the specified range for P_{step0} (4e-4 – 0.12 bar). By investigating this interval, the sensitivity analysis accounts for the high sensitivity of the step position to the chemical functionality of the adsorbent, ensuring that the process simulations capture the impact of varying step locations on performance indicators.

The parameter n_0 characterises the density of adsorption sites active in the low-coverage regime prior to the onset of cooperative adsorption. Physically, it controls the initial slope of the isotherm and determines the amount of CO_2 uptake achievable before propagation of the cooperative step. In step-shaped isotherms, this regime corresponds to chemisorption sites or amine functional groups that interact with CO_2 before full chain formation [34]. Increasing n_0 broadens the isotherm transition and produces a smoother uptake profile by activating a larger population of pre-step sites, while decreasing n_0 sharpens the step and confines adsorption to a narrower pressure interval. Fig. 3(a) shows that when n_0 exceeds ~0.5, the isotherm shape becomes nearly invariant, indicating saturation of pre-step adsorption sites; in the present parametrisation, the practical upper limit is ~0.58, beyond which further increases in n_0 have a negligible impact. In contrast, decreasing n_0 from 0.3 to 0.2 leads to reduced productivity and CO_2 recovery and increased SEC. Although the step pressure shifts slightly to lower values, the

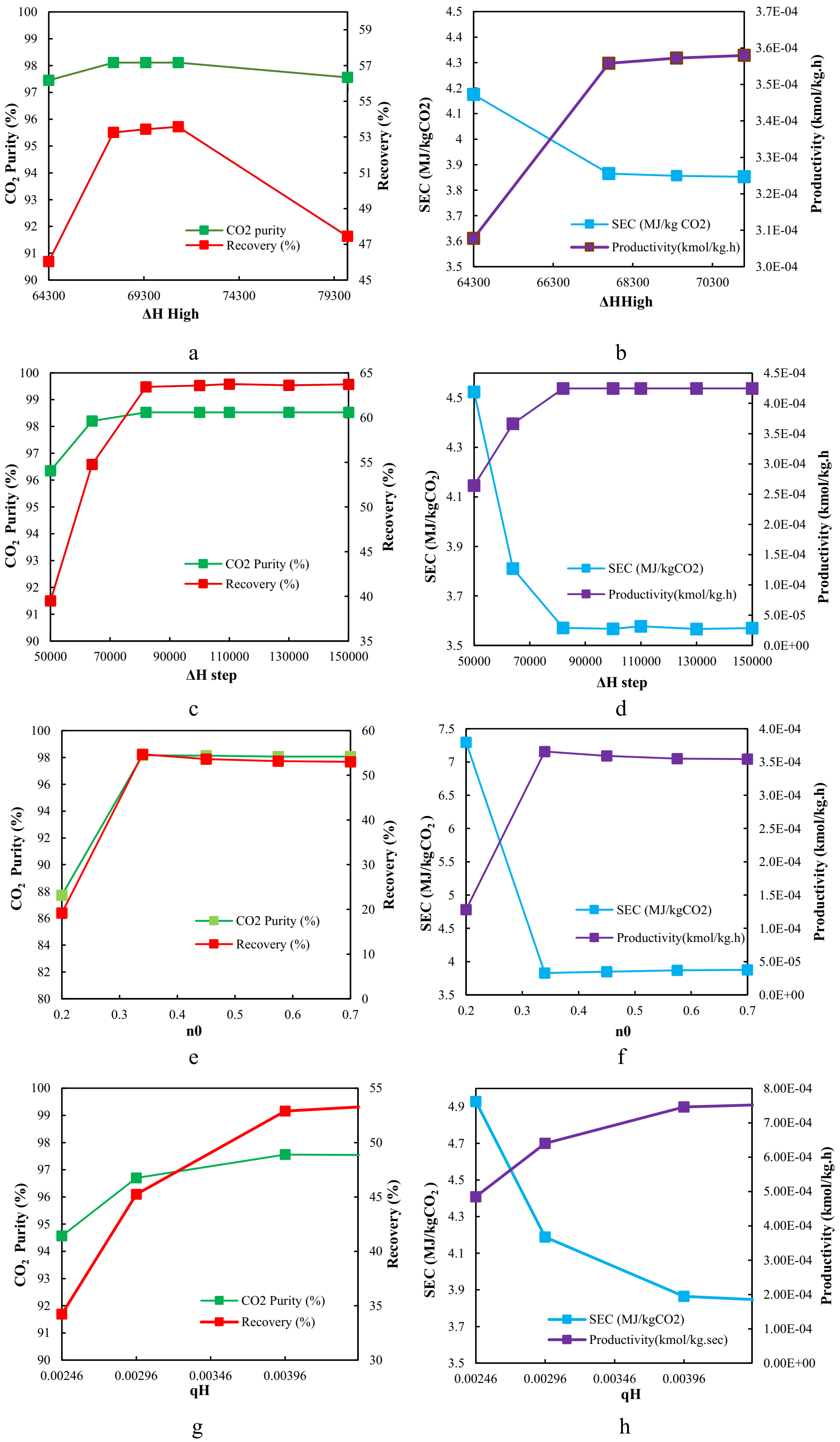

Fig. 4. Single-parameter analysis illustrating the effect of variations in different adsorbent parameters on key performance indicators from the detailed process simulation model. The green line represents CO_2 purity, the red line indicates recovery, the purple line shows productivity, and the blue line corresponds to SEC. Panels (a) and (b), (c) and (d), (e) and (f), (g) and (h) show the effect of ΔH_{High}, ΔHs_{tep0}, n_0, and $q_{H,}$ respectively.

Table 3
Selected adsorbent parameters and their corresponding ranges used in the global sensitivity analysis.

Adsorbent Parameters	Unit	Lower Bond	Upper bound
n_0	-	0.435	0.58
ΔH_{step}	kJ kmol^{-1}	−68,736	−56,242
ΔH_{High}	kJ kmol^{-1}	60,948	74,490
q_H	kmol/kg	0.00259	0.00432
ΔH_{CO2}	kJ mol-1	−80	−40
n_A	-	1.2	1.8
P_{step0}	bar	4 e-4	0.12

performance loss arises from a reduced density of nucleation sites rather than stronger CO₂ binding. A low n_0 weakens cooperative propagation, broadens the isotherm transition, and extends the induction period, thereby limiting working capacity and overall process efficiency. Similar behaviour has been reported experimentally by Darunte et al. [34] and in simulation studies [32], confirming that insufficient pre-step site density hinders efficient DAC operation.

Regarding adsorption kinetics, experimental data for mmen–Mg_2(dobpdc) shows that n_A decreases from approximately 1.7 at 95 °C to 1.0 at 55 °C, corresponding to longer induction periods near the step temperature and shorter periods at lower temperatures [37]. Based on this behaviour, the interval for n_A was set between 1.2 and 1.8 to capture the kinetic response across the relevant temperature range. Similarly, the ΔH_{CO2} range was set between 40 and 80 kJ mol^{-1}, reflecting the typical spectrum of chemisorption enthalpies for functionalised MOFs. In diamine-appended Mg_2(dobpdc) frameworks, adsorption enthalpies are typically in the range of 70 to 90 kJ mol^{-1}, while general CO_2 chemisorption enthalpies for various chemical functionalities range from 60 to 100 kJ mol^{-1}, depending on the chemical functionality [38,39]. By selecting the 40–80 kJ mol^{-1}interval, the sensitivity analysis evaluates both existing high-affinity materials and the next generation of lower-enthalpy adsorbents designed to reduce the specific energy consumption (SEC) of the regeneration step. By aligning these boundaries with established experimental limits, the resulting global sensitivity analysis captures the process response across the most relevant material design space. The conclusions of this study are expected to be robust against modest expansions of these ranges; further widening of the bounds would likely lead to physically unrealistic isotherm profiles or process conditions that exceed the operational limits of DAC. This systematic approach ensures that the evaluation of key performance indicators remains both process-relevant and consistent with the cooperative adsorption mechanism of diamine-appended Mg_2(dobpdc) materials.

2.4. Surrogate model development

2.4.1. Dataset generation and pre-processing

To generate the dataset required for the following sensitivity analysis, the Latin Hypercube Sampling (LHS) method was used. This methodological strategy systematically explores the variability of the selected input parameters within their predefined boundaries and thus produces randomised but stratified parameter vectors that guarantee uniform input space coverage [40].

An interface was developed in MATLAB to connect the LHS sampling routine with Aspen Adsorption. Specifically, the LHS algorithm creates sets of input variables, which were transferred automatically to Aspen Adsorption. For each generated case, Aspen performed a full cyclic adsorption simulation and calculated the process performance indicators, namely CO_2 purity, recovery, productivity, and SEC. Subsequently, the simulation results were exported and saved into an Excel workbook, providing a carefully organised dataset of 2866 individual cases, thereby enabling further analytical procedures. Fig. 1S illustrates the frequency distribution of each decision variable alongside normal probability density functions, confirming uniform distributions consistent with the LHS sampling method. On the other hand, the performance indicators (Fig. 2S) show that they deviate strongly from normality, as the SEC shows a right-skewed distribution, while the CO_2 purity displays a strong left tail, indicating substantial variability in the simulation results for these parameters. Logarithmic transformations were applied to skewed outputs (SEC and CO₂ purity) to improve symmetry and numerical stability. As illustrated in Fig. 5, the transformed variables exhibit distributions that more closely approximate normality.

The generated dataset was divided into training, validation, and test subsets. The partitioning strategy aimed to ensure that each subset retained the overall dataset's distribution, enabling reliable model development and unbiased performance assessment. The test set was chosen first, with roughly 10% of the entire dataset allocated for testing. To minimise random bias, multiple candidate splits (500 trials) were generated, and the test set with statistical properties, such as range, mean, and standard deviation, that most closely matched those of the full dataset was selected. This approach guaranteed that the test set would reflect the overall variability of process outputs and remain independent of model training. The remaining 90% of the data was then split into training (80%) and validation (20%) subsets. To enhance representativeness, stratified sampling based on k-means clustering of output variables was used. This ensured that both the training and validation datasets contained proportional samples from different regions of the output space, reducing the risk of the model merely learning dominant patterns and neglecting less common ones, which could compromise predictive accuracy. Due to significant differences in the magnitude of input and output variables, all variables were subsequently normalised using min-max scaling, as described in Eqs. (2) and 3, where x and y denote the original input and output values, respectively. To avoid information leakage, normalisation was performed after data partitioning, with each variable scaled to the [0, 1] range. This procedure ensured consistent transformation across all subsets while maintaining the independence of the test data.

$$x_{normalised} = \frac{x_i - x_{min}}{x_{max} - x_{min}} \tag{2}$$

$$y_{normalised} = \frac{y_i - y_{min}}{y_{max} - y_{min}} \tag{3}$$

2.4.2. ANN surrogate model configuration

A feed-forward ANN was used as a surrogate model to approximate the relationship between input parameters (P_{step0}, ΔH_{High}, ΔH_{step}, ΔH_{CO2}, n_A, n_0, and q_H) and process performance indicators (CO_2 purity, recovery, productivity and SEC). The ANN was implemented and trained using the Neural Network Toolbox of the latest version (R2024a) of the MATLAB program. The toolbox provides a comprehensive set of integrated functions that allow the definition and training of networks, and evaluating them afterwards. In the development of data-driven models such as ANN, the choice of relevant hyperparameters, i.e. the number of hidden layers, the number of neurons per layer, and activation functions, is a crucial element in the model accuracy and its generalisability. Before adopting the ANN framework, several conventional regression methods, including Linear Regression, Decision Trees, Random Forest, Support Vector Regression (SVR), and AutoML-based approaches, were systematically evaluated. The results of this comparative analysis are summarised in Tables S2–S5 of the Supplementary Information. Although these models provide useful baseline predictions, their performance remains limited, particularly in capturing certain key output variables. In particular, significant deviations were observed in the prediction of purity, highlighting the inability of these methods to fully represent the complex and highly non-linear relationships inherent in the TVSA process. These limitations motivate the adoption of the ANN model, which offers greater flexibility and modelling capacity to accurately describe such nonlinear behaviour.

In this study, to determine the optimal network architecture, a

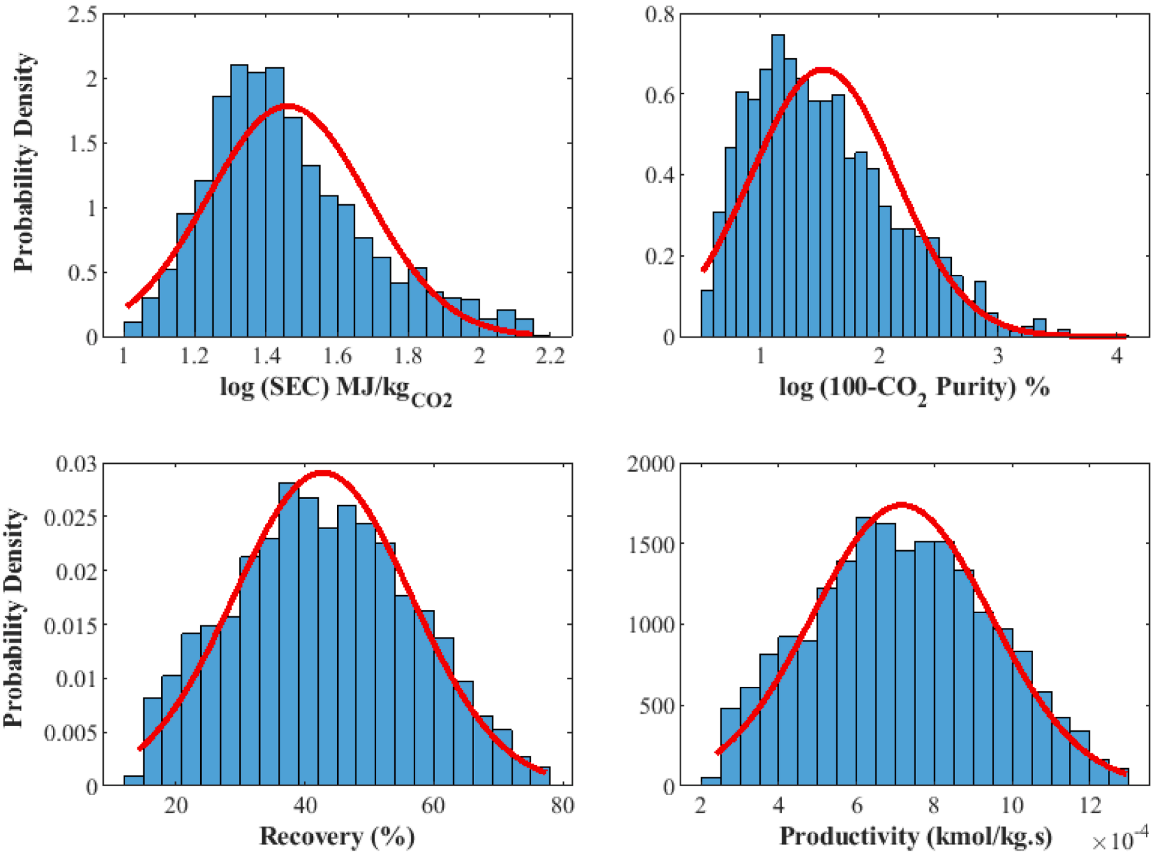

Fig. 5. Probability density distributions of process performance indicators (SEC, CO_2 purity, recovery, and productivity) after applying the logarithmic transformation.

Genetic Algorithm (GA) was employed to optimise the number of hidden layers, the neurons per layer and the activation function. The search space was constrained to a maximum of three hidden layers with a decreasing funnel neuron configuration to prevent excessive model complexity. Each candidate architecture was trained using the Levenberg-Marquardt backpropagation algorithm (trainlm) using the training dataset and then testing the performance using the validation subset. To ensure robust generalisation and prevent overfitting, a multi-objective fitness function was defined based exclusively on the model's performance on a separate validation subset. This fitness function balances three critical metrics: the mean coefficient of determination (R^2), which is a measure of the agreement between the predicted and actual values for overall correlation, mean squared error (MSE), which represents the average magnitude of the prediction error for systematic error detection, and average absolute relative deviation (AARD) for percentage-based accuracy. The performance metrics defined in Eqs. (4) to 6 are determined using the following variables: y_{actual}, the actual target value obtained from process simulation; $y_{predicted}$, the value corresponding to the empirical target value predicted by the ANN; $y_{actual, ave}$, the mean of all actual target values; i, the index of the individual data points; and n, the total number of samples. Additionally, an early stopping criterion was implemented during training, where weight updates were terminated after nine consecutive validation failures. This integrated approach ensures that the resulting surrogate model maintains high physical fidelity and predictive reliability across the entire multi-dimensional design space.

The final architecture of the ANN comprised two hidden layers with 13 neurons in the first layer and 6 neurons in the second layer, both using the logistic sigmoid activation function. The output layer consisted of four neurons, which corresponded to the four different process performance indicators, and was set to a linear activation function (purelin). The network received seven input variables and mapped them to four outputs, providing a computationally efficient surrogate model, which can be used for further sensitivity and optimisation purposes.

$$R^2 = 1 - \frac{\sum_{i=1}^{n}\left(y_{actual,i} - y_{predicted,i}\right)^2}{\sum_{i=1}^{n}\left(y_{actual,i} - y_{actual,ave}\right)^2} \tag{4}$$

$$MSE = \frac{1}{n}\sum_{i=1}^{n}\left(y_{actual,i} - y_{predicted,i}\right)^2 \tag{5}$$

$$AARD = \frac{100}{n}\sum_{i=1}^{n} abs\left(\frac{y_{actual,i} - y_{predicted,i}}{y_{actual,i}}\right) \tag{6}$$

2.5. Global sensitivity analysis

Sensitivity analysis provides valuable information on the propagation of input uncertainties through the system and their effects on system performance [41]. Its main purposes include: (i) elucidating the relationships between model inputs and outputs, (ii) quantifying the extent to which uncertainties in structural parameters contribute to overall output variability, (iii) identifying the most influential parameters governing model behaviour and output magnitudes, and (iv) providing guidance for future experimental design and model refinement. In global sensitivity analysis (GSA), all parameters are varied simultaneously throughout the parameter space, which allows the evaluation of single and higher-order interaction effects on the model outputs' variability [40,42].

This study used a variance-based Sobol sensitivity analysis to determine the relative contributions of the individual input parameters, namely (P_{step0}, ΔH_{High}, ΔH_{step}, ΔH_{CO2}, q_H, n_0, and n_A), to the variance of the four major performance indicators: CO_2 purity, recovery, productivity, and SEC. The Sobol method is one of the most powerful and widely used variance-based methods for the analysis of highly nonlinear processes, such as adsorption [40]. The total variance of model outputs is separated into those arising from a particular input parameter and those arising from interactions among these parameters. First-order Sobol indices S_1 are used to measure the contribution of a single input parameter to variance, whereas the second-order index S_2 measures the variance of the combination of two input parameters. The total order Sobol indices (S_T) measure the total effect of each input variable, including the impact of all higher- order interaction effects. Consequently, the difference between total and first-order indices (S_T-S_1) can be used as an indicator of the non-linear interactions. Fundamentally, the Sobol method follows the same variance decomposition technique used for ANOVA for factorial designs, but it enhances the method by providing a measure of the contributions of each input variable and the interactions of the variables to the total uncertainty of the model output [43,44].

In practice, the input samples were generated by Sobol quasi-random sequences and scaled to the specified ranges of the parameters. Sample matrices (A, B, and $\left(A_B^i\right)_j$) were constructed following the standard quasi-Monte Carlo sampling strategy to estimate variance contributions and compute sensitivity indices [43]. The first-order and total-order Sobol indices were calculated according to Eqs. (7) and 8, where N denotes the number of Monte Carlo samples, $f(A)_j$ and $f(B)_j$ are the model outputs corresponding to the j_{th} samples of matrices A and B, and $f\left(A_B^i\right)_j$represents the model output obtained by replacing the i_{th} column of B with that of A [45]. This sampling methodology ensures a uniform coverage of the input domain; furthermore, it provides the possibility to decompose variance for all performance indicators accurately. All Sobol sensitivity analyses were performed by the UQLab framework implemented in the MATLAB software environment, where the framework was integrated with the ANN surrogate model to efficiently evaluate system responses over the multi-dimensional parameter space.

$$S_i = \frac{\frac{1}{N}\sum_{j=1}^{N} f(A)_j f\left(A_B^i\right)_j - f(Bj))}{Var(Y)} \tag{7}$$

$$S_{Ti} = \frac{\frac{1}{2N}\sum_{j=1}^{N} \left(f(A)_j - f\left(A_B^i\right)_j\right)^2}{Var(Y)} \tag{8}$$

3. Results and discussion

3.1. *Surrogate model performance*

A single multi-output ANN surrogate model was developed to simultaneously predict CO_2 purity, recovery, productivity, and specific energy consumption. Table 4 summarises the performance of the surrogate model in terms of R^2, MSE, and AARD. Fig. 6 presents the predicted versus actual values for the four performance indicators for the validation and test datasets, while the corresponding results for the training dataset are shown in Figure S3. Recovery, productivity, and SEC are predicted with very high accuracy, achieving R^2 values above 0.98 across training, validation, and test datasets, with low MSE and AARD values. The points in the scatter plots closely align with the 45° line, indicating minimal deviation from the true values and confirming that the surrogate model generalises well beyond the training data. In contrast to recovery and productivity, which are the simplest performance indicators as they only involve the amount of CO_2 recovered, the mass or volume of the adsorbent, and the cycle time (in the case of productivity), CO_2 purity is more challenging to predict. The R^2 values for CO_2 purity are slightly lower than other indicators but remain above 0.90. This is primarily attributed to the left-skewed distribution of purity in the dataset (skewness is −2.28), where most values cluster at high purities, and only 110 out of 2866 samples (∼ 4%) fall below a purity of 85%. To evaluate the impact of this skewness on model reliability, a targeted uncertainty analysis was performed for two regimes: purities below 85% and purities above 85% (Table S6 and Figure S4).

The results demonstrate that while prediction uncertainty increases in the data-sparse, low-purity region, the model remains exceptionally certain and accurate for values exceeding 85%. Crucially, for practical Carbon Capture and Utilisation/Storage (CCUS) applications, purities exceeding 94–95% are typically required. Since the surrogate model demonstrates its highest precision in this high-purity regime, its predictive utility remains robust despite the overall statistical skewness.

Fig. 7 shows the residuals of the surrogate model predictions for the test dataset, plotted as the difference between predicted and actual values versus the actual values for each performance indicator. While the residuals generally scatter around the horizontal zero line, indicating minimal overall bias, a specific deviation is observed at high recovery (>70%) and high productivity (>1.2e-3 kmol/kg.s) values. To evaluate the reliability of the model in these critical high-performance regimes, a targeted uncertainty analysis was conducted (Table S2). The results indicate that despite the slight visual deviation in the parity plots, the model remains highly certain and reliable and is appropriate for subsequent global sensitivity analysis.

3.2. *Global sensitivity analysis (GSA)*

3.2.1. *First-order and total-effect Sobol index (main effects)*

The rankings of input parameters' importance and the consistency of these rankings across different performance indicators are illustrated in Fig. 8. In this figure, the highest rank is represented by 1 (blue) and the lowest by 7 (red). Among all investigated variables, the step pressure (P_{step0}), the adsorption enthalpy at high loading (ΔH_{High}), and the enthalpy change associated with the cooperative adsorption step (ΔH_{step}) consistently emerge as the most influential parameters. Parameters associated with adsorption kinetics (n_A) exhibit a moderate rank, while cooperative adsorption at low coverage (n_0) and ΔH_{CO2} consistency have the lowest rankings, confirming their negligible direct impact on the total variance of system outputs. From a thermodynamic perspective, while n_A modulates the kinetics toward the equilibrium, the actual cyclic working capacity is dominated by the isotherm parameters P_{step0}, ΔH_{step}, and ΔH_{High}. However, this conclusion is conditional on the operating regime. In scenarios involving significantly shorter cycle times or lower desorption temperatures, kinetic limitations could become critical. In such high-frequency operations, increased kinetics rates (characterised by higher k_A and lower effective n_A) would be required to prevent restrictions on productivity and an increase in SEC.

Table 4
Values of error metrics (R^2, MSE, and AARD) of the ANN model for four process performance indicators (SEC, CO_2 purity, recovery, and productivity) across training, validation, and test datasets.

Process parameters	Unit	Training			Validation			Test		
		R^2	MSE	AARD	R^2	MSE	AARD	R^2	MSE	AARD
SEC	MJ/kg $_{CO2}$	0.979	0.0239	1.22%	0.973	0.0297	1.29%	0.983	0.0204	1.13%
CO_2 purity	%	0.94	1.0197	0.36%	0.826	2.9061	0.48%	0.916	1.3913	0.36%
Recovery	%	0.999	1.3327	0.59%	0.984	2.2146	1.94%	0.993	1.3785	1.62%
Productivity	kmol/kg.s	0.992	0	1.54%	0.985	0	1.9%	0.993	0	1.59%

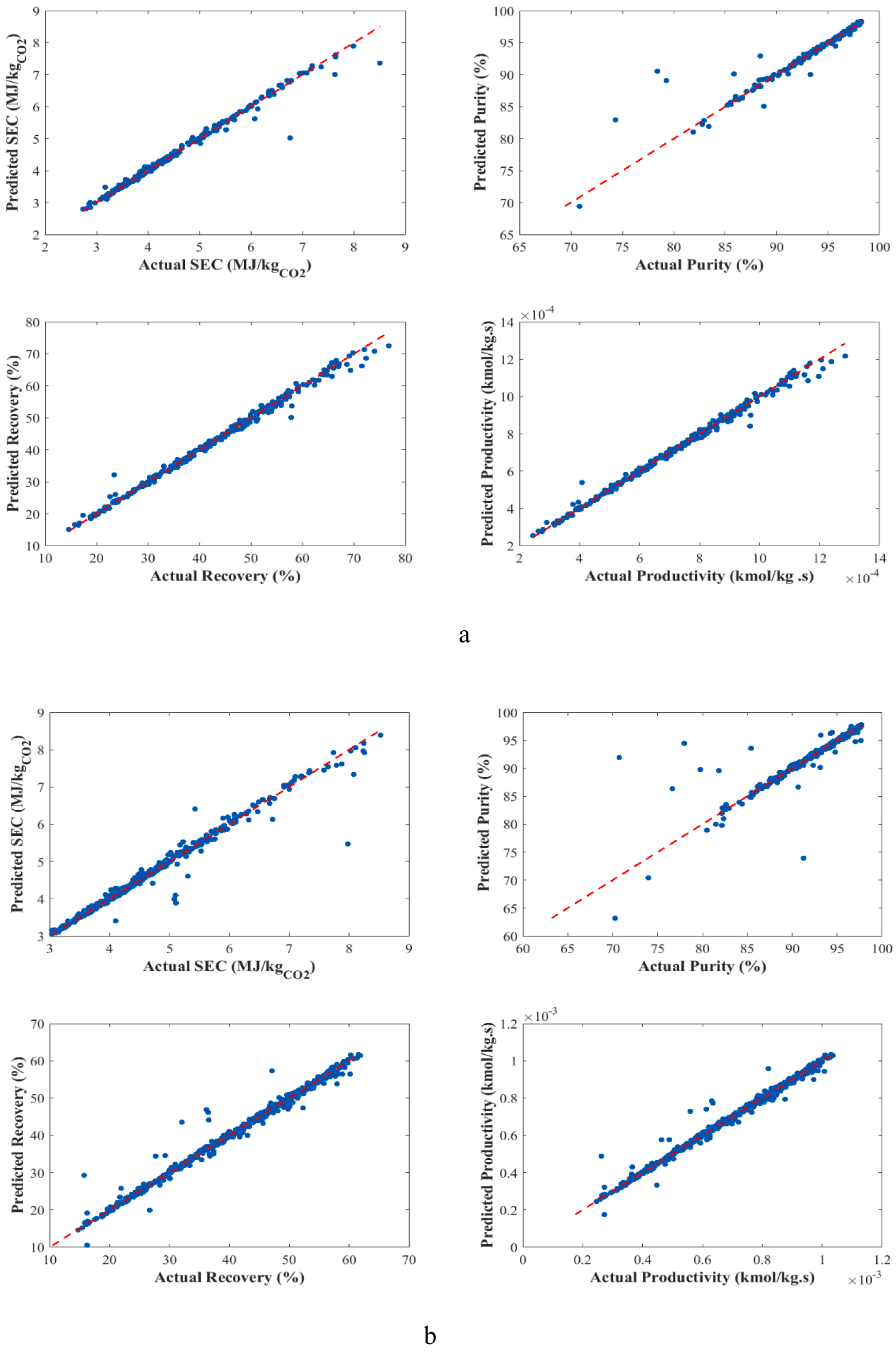

Fig. 6. Comparison between actual values (from detailed simulations) and predicted values (from the ANN model) for the four process performance indicators: SEC, CO_2 purity, recovery, and productivity. Panels (a),(b), correspond to the validation and test datasets, respectively.

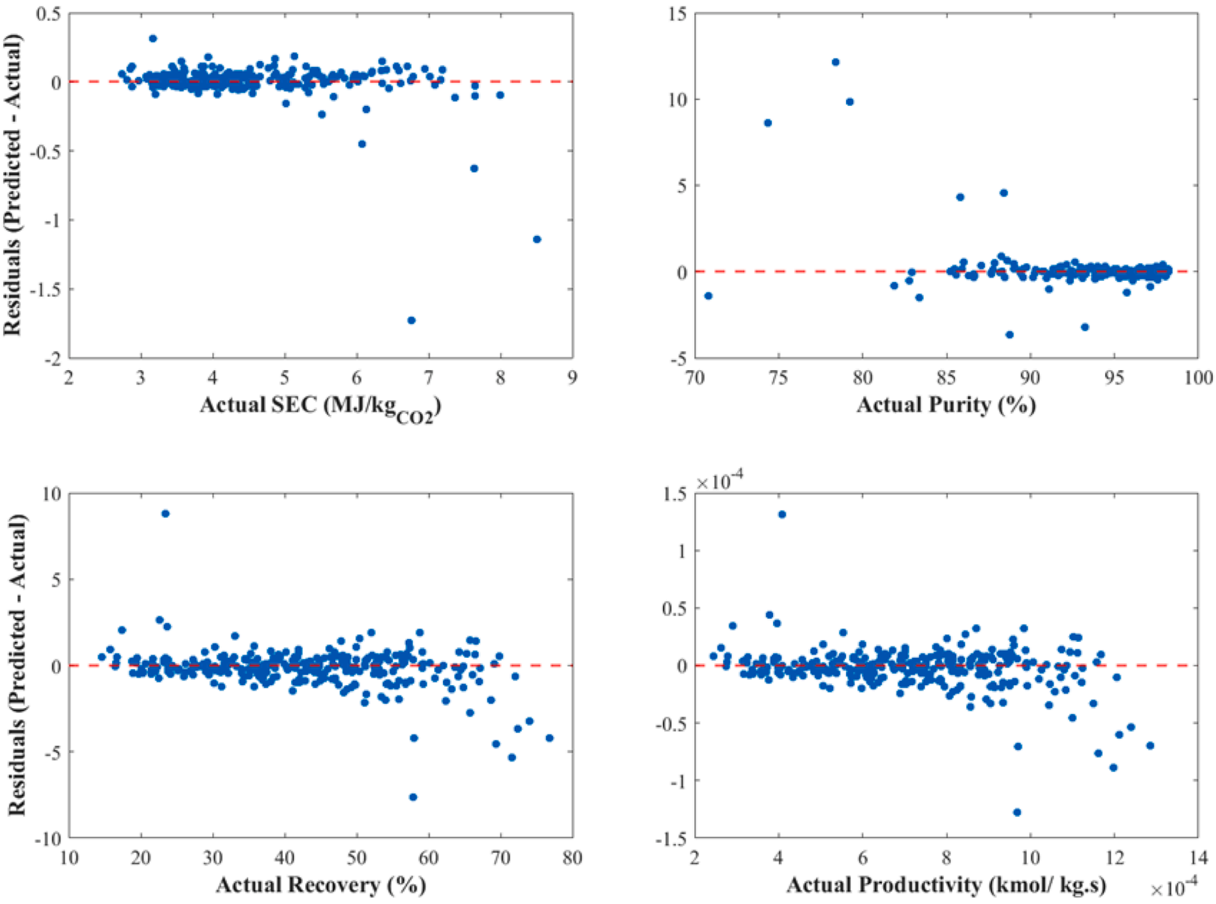

Fig. 7. Residual analysis for the test dataset, showing the difference between predicted value (from the ANN) and Actual values (from detailed simulations) for the four performance indicators: CO_2 purity, recovery, SEC, and productivity.

Therefore, while n_A didn't have the highest rank in the current baseline configuration, they may play a vital role in a cycle designed for rapid switching.

Fig. 9 shows the Sobol variance decomposition, which further supports these results by partitioning the total variance into the main effect (S_1, which is shown as the blue bars) and the interaction effect (S_T-S_1, which is shown as the orange bars). The variability found in SEC, CO_2 purity, recovery and productivity is attributed mainly to three parameters: P_{step0}, ΔH_{High}, and ΔH_{step}, which all exhibit high total order indices, usually greater than 0.40, for the majority of response variables. Conversely, the total-order indices of ΔH_{CO2}, n_0, and n_A are very low for most of the indicators, with two notable exceptions. First, n_A exhibits an S_T value greater than 0.15 for CO_2 purity, while S_1 remains near zero. This observation confirms that the influence of n_A on CO_2 purity is mainly through its interaction with other parameters rather than a direct effect. Second, ΔH_{CO2} shows a total-order index close to 0.1 for SEC, with the majority of this contribution arising from the first-order effect (S_1), indicating that its impact on SEC is largely independent of other parameters. The decomposition of S_T demonstrates that the interaction contribution (S_T-S_1) is especially important for P_{step0}, ΔH_{High}, and ΔH_{step}. This is pronounced for ΔH_{step} and P_{step0} in the case of CO_2 Purity, where interaction contributions account for more than half of the total variance, defining the selectivity-regeneration trade-off. Thermodynamically, this reflects the Van 't Hoff dependence, where ΔH_{step} dictates the temperature-induced shift of the step position (P_{step0}) required for effective regeneration. A mismatch between these parameters results in high residual CO_2 loading or a dispersive (rather than self-sharpening) breakthrough front. Both phenomena increase gas-phase mixing with inert species, significantly degrading the molar purity of the captured CO_2 stream

These results show that process performance is not determined by independent parameter effects, but by synergistic coupling, such that the optimisation of P_{step0} has to be considered in conjunction with the variation of ΔH_{step} in order to achieve meaningful improvement. Furthermore, it reveals that recovery (%) and productivity (kmol/kg·h) share nearly identical sensitivity profiles.

The near equivalence of the S_1 and S_T indices indicates a high degree of collinearity between these performance indicators, suggesting they are governed by the same dominant parameters within the defined design space. This alignment confirms that improvements in recovery inherently translate to corresponding gains in productivity. Consequently, productivity is utilised as the primary representative metric in the subsequent discussion, as the observed parameter dependencies and trends are equally applicable to recovery.

3.2.2. *Second-order Sobol index (pairwise interaction effects)*

The analysis of the second-order interaction index (S_2), shown in Fig. 10 provides additional quantitative evidence of parameter interactions. Among all pairwise interactions, the interaction between ΔH_{step} and P_{step0} is consistently the most significant, with a pronounced effect on CO_2 purity. In particular, the S_2 index for the ΔH_{step}-P_{step0} pair reaches its maximum value in this output, suggesting that the predominant portion of the interaction-driven variance (S_T-S_1) can be attributed to this synergistic association. This dominance stems from the fact that these parameters collectively define the sharpness of the phase transition; a more vertical step allows for higher CO_2 capture at lower partial pressures, which effectively narrows the mass transfer zone and minimises the co-adsorption or entrapment of impurities, thereby

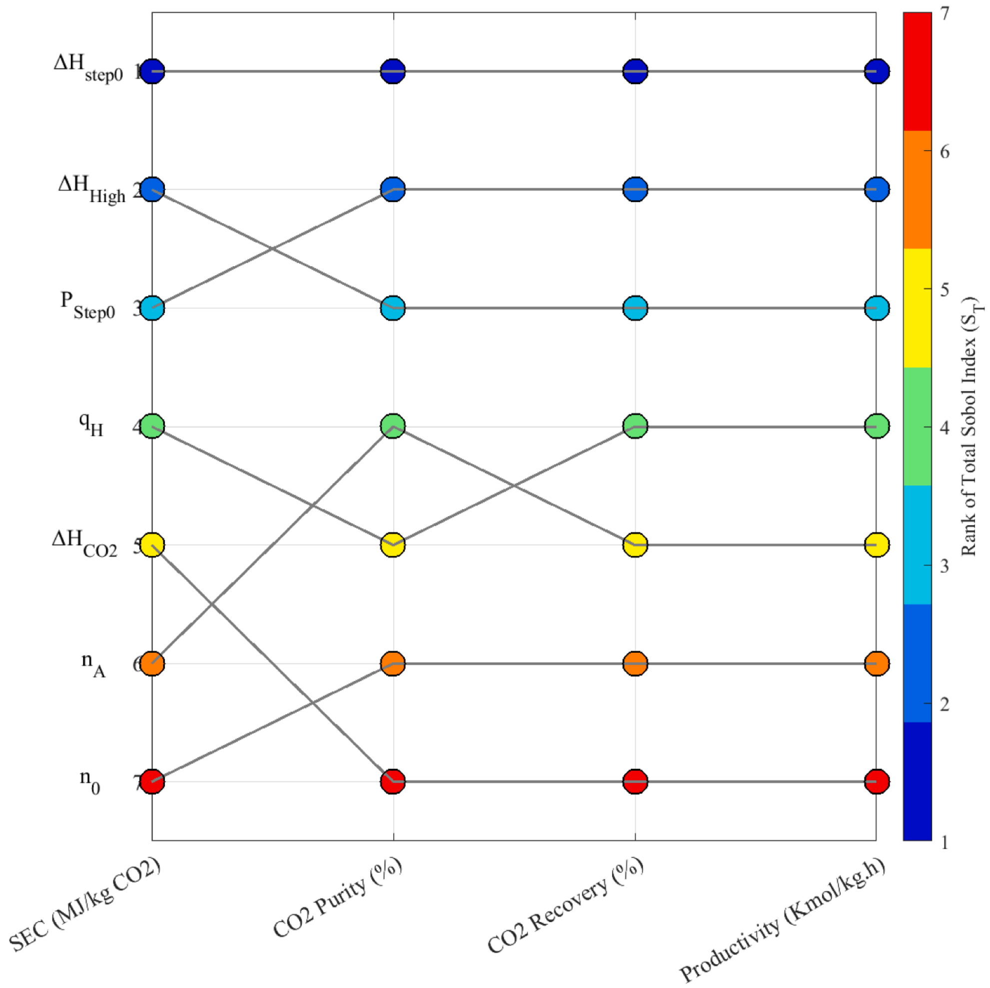

Fig. 8. Ranking of total Sobol indices across all input variables for each performance indicator, illustrating the relative importance of each parameter on CO_2 purity, recovery, productivity, and SEC.

maximising purity. The results highlight the need for design and optimisation of adsorbent properties to strictly incorporate the coupled, non-additive interactions of isotherm parameters to represent and enhance DAC performance. The second-order Sobol indices highlight significant interactions between q_H and the parameters governing the position and steepness of the cooperative step. For SEC, the strongest interactions occur with n_A, ΔH_{CO2}, ΔH_{High}, and P_{step0}, reflecting a coupled dependence of energy consumption on both total capacity and adsorption energetics. For purity, relevant interactions involve n_0, ΔH_{High}, and P_{step0}, which together influence selectivity and desorption completeness. For productivity, q_H interacts notably with n_0, ΔH_{High}, ΔH_{step}, and P_{step0} as these combinations govern the effective cyclic working capacity and overall throughput. While the first-order indices confirm that n_0 exerts a negligible direct effect, these second-order results reveal that its modest influence arises indirectly through coupling with the thermodynamic parameters governing the onset and sharpness of the cooperative transition. Specifically, the interaction between n_0 and P_{step0} reflects their shared role in defining the isotherm shape just before the step, which determines how the cooperative uptake develops.

In the current global Sobol sensitivity analysis, n_0 was varied within a narrower range (0.4–0.6), consistent with literature reports by Miller et al. [46] and Siegleman et al. [16], which indicate that n_0 remains largely invariant for mmen-Mg_2(dobpdc) when modifying the diamine structure. In these materials, structural functionalisation primarily affects the cooperative adsorption onset (P_{step0}) and the CO_2 adsorption enthalpy, whereas the pre-step region, represented by $n_{0,}$ is dominated by weak, non-specific CO_2 interactions, resulting in similar low-pressure isobars across different variants. As expected, the first-order Sobol indices indicate that n_0 exerts a negligible direct effect within this limited range, suggesting that other parameters, particularly P_{step0}, ΔH_{step}, and ΔH_{High}, dominate the process variability. However, second-order Sobol indices reveal small but measurable interaction effects, specifically between n_0 and P_{step0}, and to a lesser extent with ΔH_{step}, ΔH_{High}, and q_H. These interactions suggest that the modest influence of n_0 arises indirectly through its coupling with thermodynamic parameters that govern the isotherm shape and step position. The pronounced interaction with P_{step0} reflects their shared role in determining the sharpness and position of the cooperative step, which directly impacts working capacity and energy efficiency. Regarding SEC, n_0 exhibit only negligible effects, consistent with the dominance of enthalpy-driven energy requirements. Conversely, both productivity and purity are more sensitive to the evolution of the cooperative transition, and explain the observed connectivity between n_0 and the rest of the adsorption characteristics.

3.3. *Influence of adsorbent parameters on DAC performance*

Fig. 11 presents mmen-Mg_2(dobpdc) DAC performance in terms of productivity and specific energy consumption, where each point represents a single simulated adsorbent design satisfying CO_2 purity above 95%, P_{step0} (panel a), ΔH_{step} (panel b), ΔH_{High} (panel c), q_H (panel d), ΔHCO_2 (panel e), n_A (panel f), and n_0 (panel g) for cases with CO_2 purity

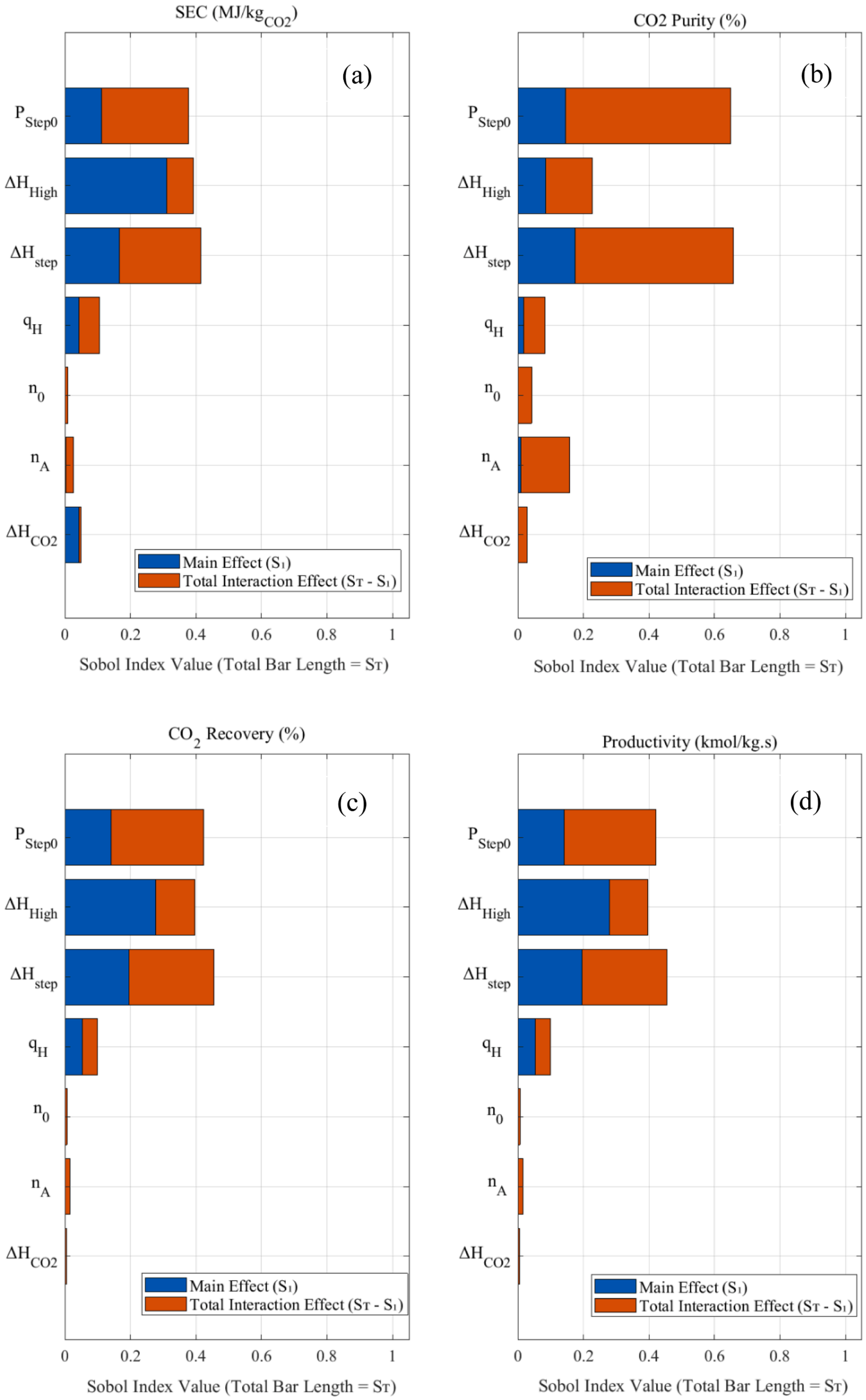

Fig. 9. Sobol variance decomposition for (a) SEC, (b) CO_2 purity, (c) recovery, and (d) productivity. The stacked bars represent the first-order Sobol indices (S1, blue) and total interaction effects (ST-S1, orange) for each input parameter.

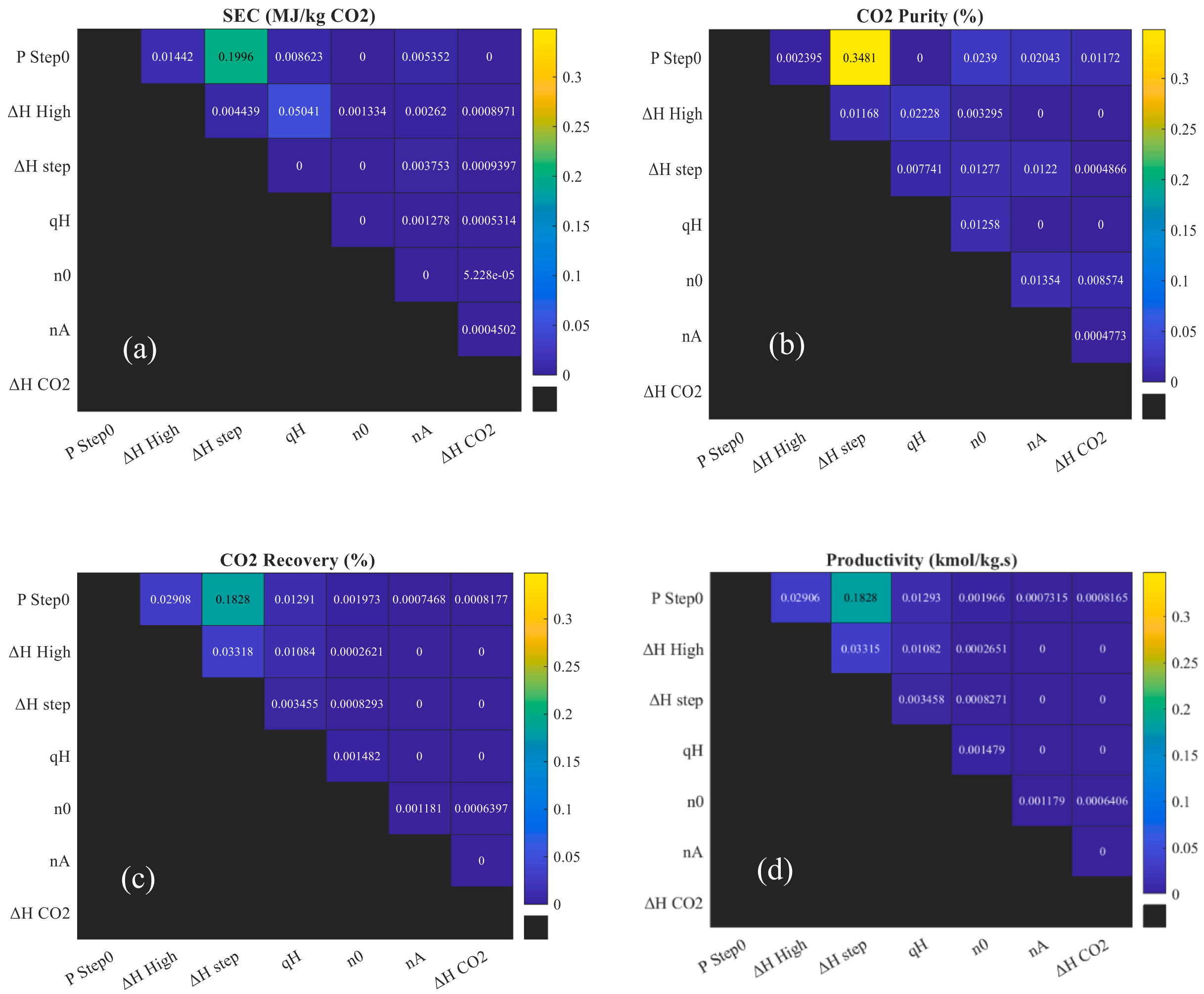

Fig. 10. Second-order Sobol sensitivity heatmaps illustrating pairwise interactions between input parameters for each performance indicator: (a) SEC, (b) CO_2 purity, (c) recovery, and (d) productivity. The colour intensity represents the magnitude of the interaction effect, with higher values indicating stronger parameter coupling.

above 95%, where SEC is represented by the colour scale and the scatter of points reflects the feasible design space explored. A strong synergistic relationship exists between productivity and SEC, indicating that higher productivity generally corresponds to lower energy consumption. Given a constant cycle time and adsorbent weight, productivity is proportional to working capacity; therefore, minimisation of SEC is equivalent to maximisation of thermodynamic efficiency.

The step pressure P_{step0} defines a narrow design window for achieving low specific energy consumption. As shown in Fig. 11(a), the optimal region is concentrated in designs with P_{step0} below approximately 5 × 10^{-4} bar, where SEC predominantly lies in the range of ~2.5–3.5 MJ/kgCO_2. Designs with higher P_{step0} are associated with progressively higher SEC, with most cases exceeding 5 MJ/kgCO_2, indicating inefficient capture under dilute DAC conditions. Conversely, designs with extremely low P_{step0} strengthen adsorption beyond the optimal range, which includes a high-SEC branch corresponding to negligible working capacity. By exploring an extensive range of P_{step0} values, this study moves beyond the simplistic assumption that a reduction in step pressure monotonically improves performance. While the high step pressure prevents adsorption under dilute DAC conditions, as the chemical potential of CO_2 in the air is insufficient to trigger the step, an excessively low step pressure shifts the equilibrium so far toward adsorption that it causes CO_2 to bind too strongly, leading to premature saturation, wasted working capacity, and inefficient regeneration [16]. This investigation effectively captures the thermodynamic trade-offs of the step position, identifying a narrow operational window where adsorption affinity and desorption propensity reach an optimal equilibrium.

As shown in Fig. 11(b), the optimal region is associated with designs having ΔH_{step} values below approximately −6.4 kJ mol^{-1}, where SEC lies within the optimal window. Designs with more exothermic ΔH_{step} values are increasingly associated with higher SEC, with many cases exceeding 5 MJ/kgCO_2, indicating inefficient regeneration. At a strongly exothermic ΔH_{step}, a distinct high-SEC branch appears, corresponding to designs in which CO_2 release is strongly suppressed. These results show that ΔH_{step} must be sufficiently weak to access the optimal regime, particularly when combined with low step pressure. The ΔH_{High} defines a clear range associated with low specific energy consumption. As shown in Fig. 11(c), the optimal region is dominated by designs with ΔH_{High} above approximately 6.7 × 10^4 kJ $kmol^{-1}$, whereas designs with lower ΔH_{High} values (≈ 6.2–6.6 × 10^4 kJ $kmol^{-1}$) are predominantly associated with higher SEC outside the optimal window. Designs with high ΔH_{High} also appear in a separate high-SEC branch, showing that elevated ΔH_{High} alone is not sufficient to guarantee low energy consumption. These results indicate that high ΔH_{High} enables access to the optimal regime only when combined with a low step pressure and ΔH_{step} values lower than moderate. The synergistic coupling between ΔH_{High} and ΔH_{step} governs more than just capacity; it dictates the steepness and width of the cooperative transition zone. From a mass-transfer perspective, a steeper transition zone produces a sharper breakthrough front. This minimises the length of the mass transfer zone (MTZ), maximising bed utilisation and preventing early CO_2 leakage—thereby

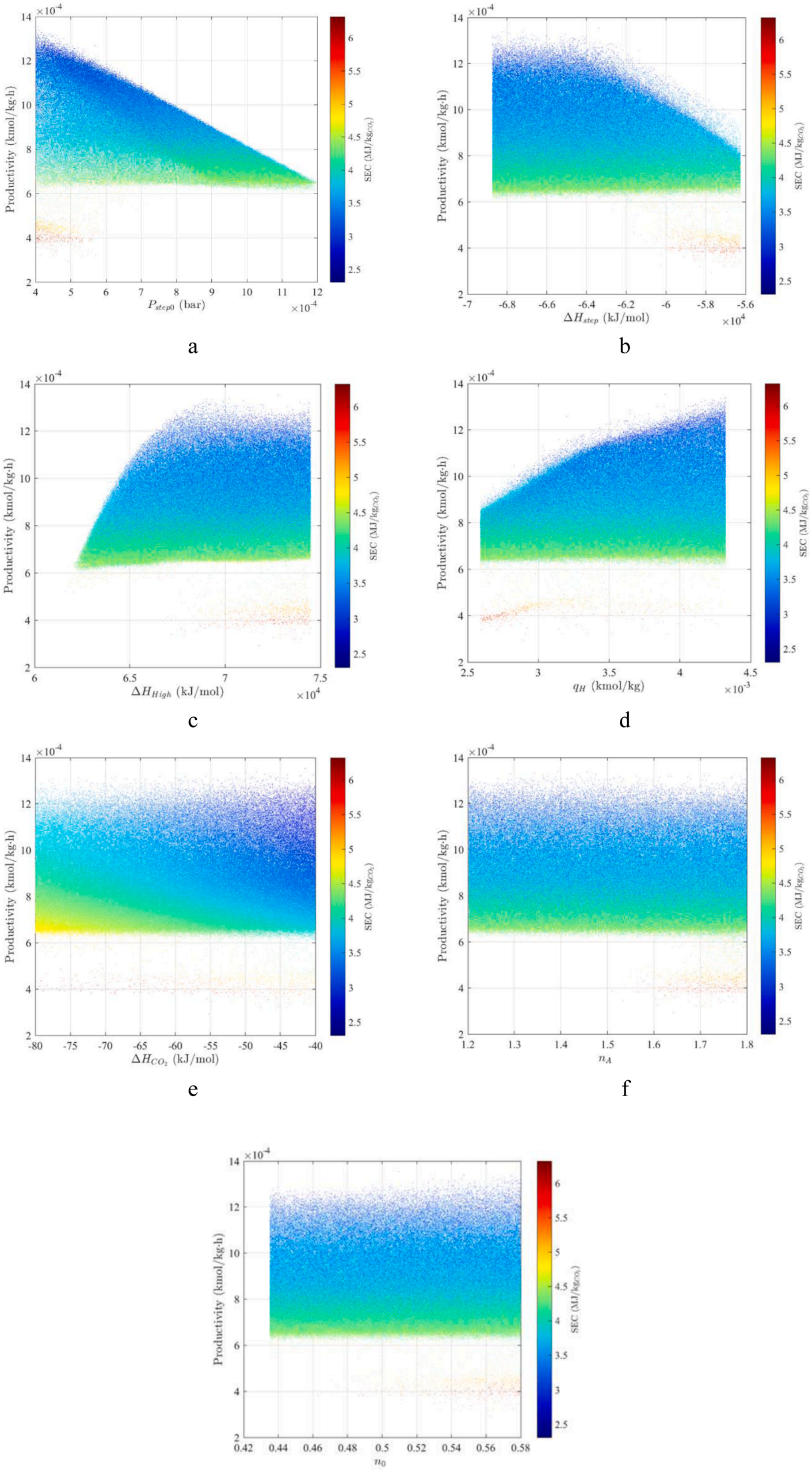

a

b

c

d

e

f

g

Fig. 11. Presents Mg_2(dobpdc) DAC performance in terms of productivity and specific energy consumption, where each point represents a single simulated adsorbent design satisfying CO_2 purity above 95%, P_{step0} (panel a), ΔH_{step} (panel b), ΔH_{High} (panel c), q_H (panel d), ΔHCO_2 (panel e), n_A (panel f), and n_0 (panel g) for cases with CO_2 purity above 95%, where SEC is represented by the colour scale and the scatter of points reflects the feasible design space explored.

explaining why specific combinations of these enthalpies are required to access the high-productivity/low-SEC regime [34].

As shown in Fig. 11(d), the optimal region for high productivity is predominantly characterised by q_H values above approximately 4 mol/kg, consistent with the increased working capacity required per cycle. Physically, q_H represents the total number of available adsorption sites once all cooperative interactions are fully activated. Therefore, designs with lower q_H ($\approx$ 2.5–3.0 mol/kg) are more frequently associated with lower productivity and higher SEC, often exceeding 5 MJ/kgCO$_2$, because the insufficient working capacity fails to offset the fixed thermal energy required to regenerate the bed.

The CO₂ adsorption enthalpy (ΔH_{CO_2}) exerts a secondary but measurable influence on specific energy consumption, providing a process-level quantification of the enthalpy–entropy trade-off characteristic of cooperative adsorbents. As shown in Fig. 11(e), designs in the optimal region are predominantly associated with lower ΔH_{CO_2} magnitudes (40 - 55 kJ mol^{-1}), whereas higher ΔH_{CO_2} values (~60–80 kJ mol^{-1}) are more frequently linked to elevated SEC, reflecting increased regeneration energy requirements. However, low ΔH_{CO_2} alone is not sufficient to ensure access to the optimal regime, as favourable performance is achieved only when combined with appropriate step pressure and step energetics. This compensatory relationship reflects the inherent physics of cooperative adsorption: stronger binding (more negative ΔH_{CO_2} shifts the step pressure to lower values, facilitating capture at ultra-dilute concentrations but increasing the thermal penalty for desorption. Conversely, weaker adsorption raises P_{step0} while improving regenerability [16]. Consequently, tuning ΔH_{CO_2} within the 40–80 kJ mol^{-1} range provides an effective molecular design strategy for expanding the operational window of cooperative adsorbents without incurring a significant energy penalty.

Fig. 11(f) shows that designs spanning the full n_A range (1.2–1.8) exhibit no systematic influence on specific energy consumption or productivity within the explored design space, with no distinct clustering observed. This observation further supports the fact that energy efficiency is mainly governed by the thermodynamic properties of the adsorbent (P_{step0}, ΔH_{step}, and ΔH_{High}) rather than kinetic parameters (n_A) under the defined process conditions. This behaviour is attributed to the fact that the TVSA cycle durations are sufficiently long to allow the bed to reach equilibrium during both adsorption and desorption. As noted by Martell et al. [35], the time required to reach equilibrium within the experimentally relevant n_A range is modest relative to typical process timescales. Because the induction period, where n_A dictates the nucleation and growth pathway, is significantly shorter than the total step duration, the internal mechanistic pathway does not limit the final working capacity. Furthermore, the overall capture rate is likely governed by external mass transfer or the global rate constant (k_A), rather than the internal growth dimensionality represented by n_A. Consequently, the system operates in a regime where the final state of the bed and the overall mass of CO$_2$ exchanged are determined by thermodynamic equilibrium rather than the specific kinetic pathway of the cooperative transition. Similarly, the desorption step is sufficiently long to ensure complete bed regeneration, placing the regeneration half-cycle equally within an equilibrium-controlled regime. As a result, kinetics exert negligible influence over both half-cycles, and overall process performance remains governed by thermodynamic properties throughout. In Fig. 11(g), a similar weak and diffuse dependence is observed across the full n_0 range (0.44–0.58), which indicates low-loading isotherm curvature has a limited impact on process performance under the cycle conditions considered. This is consistent with literature reports [16,46] suggesting that structural functionalization in these materials primarily affects the cooperative adsorption onset $P_{step0,}$ and the CO$_2$ adsorption enthalpy. In contrast, the pre-step region represented by n_0 is dominated by weak, non-specific CO$_2$ interactions, resulting in nearly identical low-pressure isobars across different material variants.

Overall, the results in Fig. 11 indicate that the optimal region is achieved when lower P_{step0} (< 0.7 mbar), moderately exothermic ΔH_{step} (< −6.6 kJ mol^{-1}), strongly exothermic ΔH_{High} (> 7.2 kJ mol^{-1}), higher qH (>4 mol/kg), and DH_{CO2} between 40 - 55 kJ mol^{-1}. These values correspond closely to high-performance analogues such as dmpn-Mg$_2$(dobpdc), which strikes a balance between high affinity and modest temperature swing requirements [46]. These results quantitatively delineate the adsorbent property ranges required for efficient DAC operation and provide direct guidance for cooperative isotherm design.

4. Optimal isotherm design

A representative candidate from the high-performance region identified through the Global Sensitivity Analysis (GSA) in Fig. 12 was selected to demonstrate the potential for performance enhancement under identical process conditions. This tailored case, derived from the GSA-informed design space, illustrates the specific shifts in adsorbent descriptors required to maximise DAC efficiency. The corresponding parameters and their percentage deviations from the base case are summarised in Table 5. The most noticeable change from the original is a decrease in P_{step0} by about half, followed by the moderate changes in q_H and ΔH_{CO2}. In contrast, parameters n_0 and ΔH_{Hig} show the smallest deviations. These variations modify the adsorption step and the high-loading capacity, therefore, affecting SEC, productivity and CO$_2$ purity. Although the Sobol sensitivity analysis identifies ΔH_{High} and ΔH_{step} as influential parameters, their variation between the base and optimised cases is relatively small. The outcomes reflect that the base-case values are in the thermodynamically favourable range: the value of ΔH_{High} was found to be around 7e4 - 7.5e4 kJ kmol^{-1}, whereas ΔH_{step} is in the range from −6.5e4 to −7e4 kJ kmol^{-1}. Both parameters (ΔH_{step} and ΔH_{High}) have an impact on the position and slope of the cooperative step. ΔH_{step} mainly shifts the step position without substantially altering the slope, whereas ΔH_{High} modifies both the slope and the high-loading region of the isotherm. In contrast, the direct adjustment of P_{step0} is the most effective approach, which can be used, as it perfectly aligns the cooperative step with the process operating pressures. Consequently, the most significant performance improvement in the selected case is due to the reduction of P_{step0}. Additionally, small adjustments in ΔH_{step} and ΔH_{High} are used to refine the isotherm configuration, and therefore enhance the working capacity and reduce the SEC.

This combination effectively mitigates the traditional trade-off between energy efficiency and capture rate that is usually present in physisorbents or noncooperative chemisorbents. The physical basis for this synergy lies in the cooperative mechanism of adsorption: a steep step at low pressure allows reaching large working capacities per cycle, while a careful balance between the enthalpic interactions (ΔH_{step} and ΔH_{High}) permits achieving an efficient regeneration without excessive heat duty. The minimal change in n_0 between the baseline and optimised conditions is another indication of its low impact on process results. Experimental investigations on diamine-appended Mg$_2$(dobpdc) indicate that even though diamine substitution causes a significant change in the cooperative step pressure (P_{step0}) and the adsorption enthalpy, the low-pressure regime, represented by n_0, remains largely unchanged once pre-step sites are saturated [16,46]. The observed invariance accounts for the negligible first- order sensitivity of n_0 measured in the global Sobol analysis in the 0.4–0.6 range. Nevertheless, local sensitivity analysis demonstrates that reducing n_0 below about 0.3 broadens the step transition, lowers the working capacity and diminishes the overall process performance. The values used in this investigation are within the optimum range for the given parameter, thus indicating that further modification of the value of n_0 is unnecessary to achieve efficient DAC performance.

Fig. 13 presents the comparison between the experimental isotherm of mmen-Mg$_2$(dobpdc) and the optimised ones obtained through the isotherm design framework developed in this study. The temperature-dependent variation of the step-shaped adsorption isotherms for the selected framework is illustrated in Fig. 5S. The process simulation

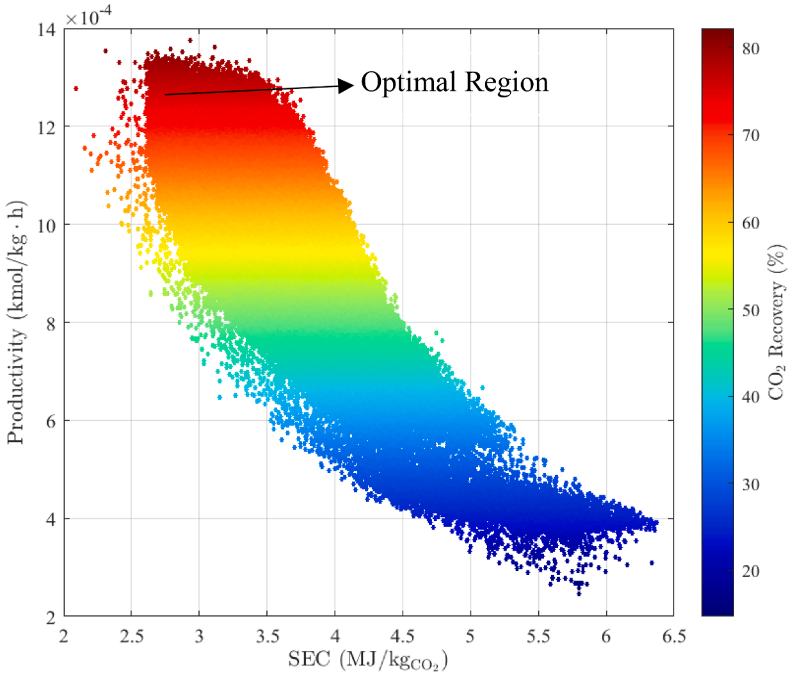

Fig. 12. Optimal region in the feasible design space.

Table 5
Optimised case parameters and their percentage differences relative to the base case.

Parameter	Unit	Initial Values	Selected Values	Changes (%)
P_{step0}	bar	0.0008	0.000419	−47.3
ΔH_{High}	kJ kmol^{-1}	67,720	67,925	+0.3
ΔH_{step}	kJ kmol^{-1}	−62,490	−67,149	−7.4
ΔH_{CO2}	MJ Kmol^{-1}	−71	−59	+16.9
n_0	-	0.518	0.5218	+0.7
n_A	-	1.5	1.27	−15.3
q_H	kmol/kg	0.00346	0.004301	+24.2

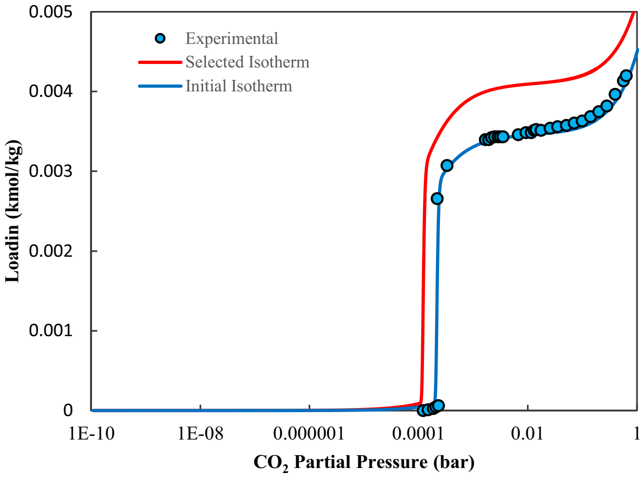

Fig. 13. Comparison of c: the blue curve represents the experimental isotherm of mmen–Mg_2(dobpdc), while the red curve corresponds to the optimised isotherm obtained from the selected parameters; Symbols represent experimental data at 25 °C [34].

results obtained using the optimised parameters are evaluated against the base case in this study. Compared with the base case, the optimised isotherm improves all major performance indicators. CO_2 recovery increases from 53.3% to 76.0%, representing a 42.7% improvement, while productivity rises from 8.69e-4 to 1.2e-3 kmol/kg.h, an increase of approximately 1.4 times. Simultaneously, the SEC decreases from 3.85 to 2.9 MJ/kgCO_2, corresponding to a 25% reduction, with CO_2 purity remaining nearly constant at around 98%. These results demonstrate that optimising the isotherm thermodynamics, primarily by lowering P_{step0} and adjusting ΔH_{CO2} and q_H within their effective ranges, can substantially improve both SEC and productivity without compromising product purity. Moreover, a comparison with the literature data relating to adsorbents with conventional isotherms shows that the optimised mmen-Mg_2(dobpdc) achieves a comparable CO_2 purity and recovery, but at a much lower SEC. The results in this article highlight the advantage of adjusting the cooperative adsorption thermodynamics to improve energy efficiency while also maintaining product quality. As all process operating conditions have been kept constant during this analysis, the observed improvement can be attributed to the modified isotherm properties. It should be noted that the SEC reported in this work is lower than the Climeworks benchmark, which is attributable to several modelling simplifications inherent to this study: pressure drop across the contactor is assumed negligible, excluding blower energy consumption; vacuum equipment is modelled at idealised efficiency; the feed stream is assumed dry, excluding the energy penalty associated with water–CO_2 separation; and structured contactor flow resistance is not considered. These factors collectively result in an underestimation of the true energy demand, and their inclusion would be expected to bring the reported SEC closer to the Climeworks reference value (Table 6).

5. Conclusion

This work provides a process-level understanding of how both thermodynamic and kinetic parameters of cooperative, step-shaped adsorption systems influence the performance of direct air capture (DAC) processes. By utilising a variance-based Sobol global sensitivity analysis on an ANN surrogate model, which was developed from a comprehensive packed-bed TVSA model, this study enables an efficient exploration of the relationship between material properties and process performance. This approach successfully quantifies the relative

Table 6
Performance comparison between the optimised case (designed isotherm) and the base case, alongside benchmark sorbents reported for DAC applications.

Case	Adsorbent	Process	Purity (%)	Recovery (%)	SEC (MJ/kgCO$_2$)	Productivity (kmol/kg.h)	Reference
Base case[a]	mmen-Mg$_2$(dobpdc)	TVSA	98.13	53.26	3.85	8.69e-4	This work
Optimal designed isotherm case[a]	mmen-Mg$_2$(dobpdc)	TVSA	98.5	76	2.9	1.2e-3	This work
Climeworks (Benchmark)[b]	Amine-functionalised	TVSA	>95	85.4	10.8	-	[47–50]
Sinha et al. 2016[cc]	mmen-Mg$_2$(dobpdc)	s-TVSA	95	60	3.52	-	[51]
Balasubramaniam et al. 2024[d]	NbOFFIVE-Ni	s-TVSA	≥95	20 - 40	30.78 - 50	-	[52]
Sabatino et al. 2021[e]	Various solid sorbents	TVSA			4.9 – 13.3	-	[53]

(a) Dry inlet air (400 ppm CO$_2$); packed bed contactor; no blower required; vacuum pump for desorption; indirect heating via single-phase jacket (no steam generation), no CO$_2$ compression.

(b) Wet inlet air (400 ppm CO$_2$); structured monolith contactor (Climeworks Mammoth); blower for adsorption; vacuum pump for desorption; direct low-grade geothermal waste heat for regeneration (~80–100°C, no steam generation), no CO$_2$ compression.

(c) Wet inlet air (400 ppm CO$_2$, 25% RH); coated monolith contactor; blower for adsorption; vacuum pump for desorption; direct steam used for desorption, no CO$_2$ compression.

(d) Wet inlet air (400 ppm CO$_2$, 50% RH); fixed bed contactor; blower for adsorption; vacuum pump for desorption; direct steam heating for regeneration; no CO$_2$ compression.

(e) Wet inlet air (400 ppm CO$_2$, 43% RH); structured monolith contactor (Climeworks Mammoth); blower for adsorption; vacuum pump for desorption; indirect heating for regeneration (no steam); CO$_2$ compression considered.

importance of individual parameters and their complex interactions, providing a robust framework for identifying the key drivers of capture efficiency and energy consumption.

The results show that DAC performance is primarily controlled by the thermodynamic positioning and strength of the adsorption step. In particular, step pressure and adsorption enthalpies govern the trade-off between energy consumption, productivity, recovery, and CO$_2$ purity, while kinetic effects play a secondary role under the studied conditions. The strong interaction between step position and adsorption strength highlights the importance of aligning the adsorption step with the process operating window. These findings demonstrate that optimal DAC performance is not achieved by maximising adsorption strength alone, but by carefully balancing adsorption capacity, regeneration energy, and kinetic effects. This provides clear design guidance for cooperative sorbents, emphasising the need to tune these parameters to match process conditions.

Overall, this work establishes a framework for linking material design to process performance, offering practical guidelines for the development of next-generation cooperative sorbents for DAC applications. However, several limitations remain to be addressed in future research. The model currently assumes ideal, dry conditions. Future work must evaluate performance under realistic humidity and long-term sorbent degradation. Additionally, while lab-scale phenomena are captured, moving to industrial-scale units will require accounting for larger heat-transfer limitations and flow non-uniformities. While this study identifies optimal isotherm targets, the chemical feasibility of synthesising materials with these exact cooperative parameters remains a vital area for experimental validation. Furthermore, a key future direction is the simultaneous optimisation of material properties and process parameters (cycle times, temperatures, and flow rates). Pairings of adsorbents with tailored cycles are necessary to move from individual material selection to a global superstructure-based optimisation.

Funding information

This research did not receive any specific grant from funding agencies in the public, commercial, or not-for-profit sectors.

CRediT authorship contribution statement

Maryam Nasiri Ghiri: Writing – original draft, Visualization, Validation, Software, Methodology, Formal analysis, Data curation, Conceptualization. **Hamid Reza Nasriani:** Writing – review & editing, Supervision, Project administration, Conceptualization. **Mohammad Bagheri:** Writing – review & editing, Visualization, Formal analysis. **Leila Khajenoori:** Supervision, Conceptualization. **Samira khani Rasmussen:** Supervision, Conceptualization. **Andrei Chamchine:** Writing – review & editing, Project administration, Investigation, Funding acquisition, Conceptualization.

Declaration of competing interest

The authors declare that they have no known competing financial interests or personal relationships that could have appeared to influence the work reported in this paper.

Supplementary materials

Supplementary material associated with this article can be found, in the online version, at doi:10.1016/j.ceja.2026.101283.

Data availability

Data will be made available on request.

References

[1] A. Gandomkar, F. Torabi, H.R. Nasriani, R. Enick, Maximising CO$_2$ sequestration efficiency in deep saline aquifers through in-situ generation of CO$_2$-in-brine foam incorporating novel CO$_2$-soluble non-ionic surfactants, Chem. Eng. J. 166102 (2025), https://doi.org/10.1016/j.cej.2025.166102.

[2] F.J. Medaiyese, H.R. Nasriani, K. Khan, L. Khajenoori, Sustainable hydrogen production from plastic waste: optimizing pyrolysis for a circular economy, Hydrogen 6 (1) (2025) 15.

[3] A.H. Idaereesoaari, Aimikhe, J. Victor, Formulation and modification of multi-walled carbon nanotubes for post-combustion CO 2 capture, Artic. Int. J. Energy Eng. 2023 (1) (2023) 13–23, https://doi.org/10.5923/j.ijee.20231301.02.

[4] D. Fu, Y. Park, M.E. Davis, Zinc containing small-pore zeolites for capture of low concentration carbon dioxide, Angew. Chem. Int. Ed. 61 (5) (2022), https://doi.org/10.1002/anie.202112916.

[5] R. Ben-Mansour, et al., Carbon capture by physical adsorption: Materials, experimental investigations and numerical modeling and simulations – a review, Appl. Energy 161 (2016) 225–255, https://doi.org/10.1016/J.APENERGY.2015.10.011.

[6] H. Liang, R. Yang, Z. Zhang, J. Wu, Y. Gao, Q. Wang, D. O'Hareb, Z. Zhong, J. Wang, Recent advances in solid sorbents for CO2 capture and new development trends, Energy Env. Sci. 7 (11) (2014) 3478–3518.

[7] J.M. van Batena, R. Krishnaa, In silico screening of metal–organic frameworks in separation applications, Phys. Chem. Chem. Phys. 13 (22) (2011) 10593–10616.

[8] L. Li, H.S. Jung, J.W. Lee, Y.T. Kang, Review on applications of metal–organic frameworks for CO2 capture and the performance enhancement mechanisms, Renew. Sustain. Energy Rev. 162 (2022) 112441, https://doi.org/10.1016/J.RSER.2022.112441.

[9] M. Tian, J. Lan, X. Cao, X. Wang, Z. Chai, J.K. Gibsone, W. Shi, L. Yuan, Defect engineering in metal–organic frameworks: a new strategy to develop applicable actinide sorbents, Chem. Commun. 54 (4) (2018) 370–373.

[10] K. Epp, W.R. Heinz, G. Kieslich, R.A. Fischer, S. Dissegna, Defective metal-organic frameworks, Adv. Mater. 30 (37) (2018).

[11] J.G. Vitillo, G. Ricchiardi, Effect of pore size, solvation, and defectivity on the perturbation of adsorbates in MOFs: the paradigmatic Mg2(dobpdc) case study, J. Phys. Chem. C 121 (41) (2017) 22762–22772, https://doi.org/10.1021/acs.jpcc.7b06252.

[12] T.M. Mcdonald, Synthesis and Characterization of Alkylamine-Functionalized Metal-Organic Frameworks as Adsorbents for Carbon Dioxide, University of Califirnia, Berkerly, 2015 [Online]. Available: https://escholarship.org/uc/item/8ph267b9.

[13] D.M. D'Alessandro, R. Krishnac, J.R. Long, T.M. McDonald, Enhanced carbon dioxide capture upon incorporation of N,N′-dimethylethylenediamine in the metal–organic framework CuBTTri†, Chem. Sci. 2 (10) (2011) 2022–2028.

[14] T.M. McDonald, et al., Cooperative insertion of CO2 in diamine-appended metal-organic frameworks, Nature 519 (7543) (2015) 303–308, https://doi.org/10.1038/nature14327.

[15] T.M. McDonald, W.R. Lee, J.A. Mason, B.M. Wiers, C.S. Hong, J.R. Long, Capture of carbon dioxide from air and flue gas in the alkylamine-appended metal-organic framework mmen-Mg 2(dobpdc), J. Am. Chem. Soc. 134 (16) (2012) 7056–7065, https://doi.org/10.1021/ja300034j.

[16] R.L. Siegelman, et al., Controlling cooperative CO2 adsorption in diamine-appended Mg2(dobpdc) metal-organic frameworks, J. Am. Chem. Soc. 139 (30) (2017) 10526–10538, https://doi.org/10.1021/jacs.7b05858.

[17] G. Rim, G. Mirzazadeh, J. Hoffman, H.J. Moon, J.E. Leisen, O.G. Nik, R.P. Lively, C. W. Jones, M.G. Song, Amine-dependent CO2 sorption on amine-impregnated Mg2 (dobpdc) MOF under humid conditions, Ind. Chem. Mater. (2025), https://doi.org/10.1039/D5IM00002E.

[18] H. Zied, S. Achour, ML-driven models for predicting CO 2 uptake inmetal–organic frameworks (MOFs), Can. J. Chem. Eng. (2024).

[19] J. Burner, L. Schwiedrzik, M. Krykunov, J. Luo, P.G. Boyd, T.K. Woo, High-performing deep learning regression models for predicting low-pressure CO2 adsorption properties of metal−organic frameworks, J. Phys. Chem. C 124 (51) (2020) 27996–28005, https://doi.org/10.1021/acs.jpcc.0c06334.

[20] M. L. C. Y. L. O. K. F. B. G. H. J. T. H., R.Q.S. Christopher E Wilmer, Large-scale screening of hypothetical metal–organic frameworks, Nat. Chem. 4 (2012) 83–89.

[21] W. Yang, X. Deng, C. Cai, Y. Yan, H. Liang, Z. Liua, Z. Qiao, Z. Shi, Machine-learning-assisted high-throughput computational screening of high performance metal–organic frameworks, Mol. Syst. Des. Eng. 5 (2020) 725–742.

[22] A. Luukkonen, J. Elfving, Optimizing direct air capture: evaluating the impact of process parameters on productivity, energy requirement, and cost [Online]. Available: https://ssrn.com/abstract=5014185, 2024.

[23] L. Joss, M. Gazzani, M. Hefti, D. Marx, M. Mazzotti, Temperature swing adsorption for the recovery of the heavy component: an equilibrium-based shortcut model, Ind. Eng. Chem. Res. 54 (11) (2015) 3027–3038, https://doi.org/10.1021/ie5048829.

[24] B.J. Maring, P.A. Webley, A new simplified pressure/vacuum swing adsorption model for rapid adsorbent screening for CO2 capture applications, Int. J. Greenh. Gas Control 15 (2013) 16–31, https://doi.org/10.1016/J.IJGGC.2013.01.009.

[25] H. R. N. L. K. K. S. W. S. M. K. E. R., M. Nasiri Ghiri, Multi-objective optimization of CO2 capture from ambient air via TVSA process modeling, in: World CCUS Conference 2025, European Association of Geoscientists & Engineers, 2025, pp. 1–5.

[26] M. Bui, N.M. Dowell, C. Petit, D. Danaci, Exploring the limits of adsorption-based CO2 capture using MOFs with PVSA – from molecular design to process economics, R. Soc. Chem. 5 (2020) 212–231.

[27] M. Nasiri-ghiri, H.R. Nasriani, L. Khajenoori, S.K. Rasmussen, K. Williams, Surrogate-assisted cyclic performance optimisation of direct air capture using amine-functionalised metal–organic frameworks, Sep. Purif. Technol. 383 (2026) 136177, https://doi.org/10.1016/J.SEPPUR.2025.136177.

[28] Y. Takakura, et al., Surrogate model optimization of vacuum pressure swing adsorption using a flexible metal organic framework with hysteretic sigmoidal isotherms, Int. J. Greenh. Gas Control 138 (2024) 104260, https://doi.org/10.1016/J.IJGGC.2024.104260.

[29] J. Young, F. Mcilwaine, B. Smit, S. Garcia, M. van der Spek, Process-informed adsorbent design guidelines for direct air capture, Chem. Eng. J. 456 (2023), https://doi.org/10.1016/j.cej.2022.141035.

[30] Y. Xie, S. Deng, X. Yuan, S. Li, Machine Learning-empowered plastic-derived porous carbons for high-performance CO2 capture, Acc. Mater. Res. 6 (11) (2025) 1319–1331.

[31] C., M. E., S. J. et al. Charalambous, "a holistic platform for accelerating sorbent-based carbon capture," vol. 632, pp. 89–94, 2024.

[32] H.E. Holmes, J. Kim, M.J. Realff, Process systems engineering: a key enabler of adsorption-based direct air capture, Curr. Opin. Chem. Eng. 51 (2026) 101202, https://doi.org/10.1016/J.COCHE.2025.101202.

[33] M.N. Ghiri, H.R. Nasriani, L. Khajenoori, S. Mohammadkhani, K.S. Williams, Dynamic temperature–vacuum swing adsorption for sustainable direct air capture: parametric optimisation for high-purity CO2 removal, Sustainability 17 (15) (2025) 6796, https://doi.org/10.3390/su17156796.

[34] L.A. Darunte, et al., Moving beyond adsorption capacity in design of adsorbents for CO 2 capture from ultradilute feeds: kinetics of CO 2 adsorption in materials with stepped isotherms, Ind. Eng. Chem. Res. 58 (1) (2019) 366–377, https://doi.org/10.1021/acs.iecr.8b05042.

[35] J.D. Martell, P.J. Milner, R.L. Siegelman, J.R. Long, Kinetics of cooperative CO2adsorption in diamine-appended variants of the metal-organic framework Mg2 (dobpdc), Chem. Sci. 11 (25) (2020) 6457–6471, https://doi.org/10.1039/d0sc01087a.

[36] J. Xu, et al., Amine dynamics in diamine-appended Mg2(dobpdc) metal-organic frameworks, J. Phys. Chem. Lett. 10 (22) (2019) 7044–7049, https://doi.org/10.1021/acs.jpclett.9b02883.

[37] P.J. Milner, R.L Siegelman, J.R Long, J.D. Martell, Kinetics of cooperative CO2 adsorption in diamine-appended variants of the metal–organic framework Mg2 (dobpdc), Chem. Sci. 11 (25) (2020) 6457–6471.

[38] P.J Milner, J.-H. Lee, H.N Redfearn, J. Ok-tawiec, R.L Siegelman, J.D Martell, B. Dinakar, L.B Porter-Zasada, M.I Gonzalez, J.B Neaton, J.R Long, J.A Reimer, A. C. Forse, Elucidating CO2 chemisorption in diamine-appended metal–organic frameworks, J. Am. Chem. Soc. 140 (51) (2018) 18016–18031.

[39] O.H.P. Gunawardene, C.A. Gunathilake, K. Vikrant, S.M. Amaraweera, Carbon Dioxide Capture Through Physical and Chemical Adsorption Using Porous Carbon Materials: a Review, MDPI, 2022, https://doi.org/10.3390/atmos13030397.

[40] M.N. Trame, L.J. Lesko, S. Schmidt, X.-Y. Zhang, Sobol sensitivity analysis: a tool to guide the development and evaluation of systems pharmacology models, CPT Pharmacomet. Syst. Pharmacol. 4 (2) (2015) 69–79.

[41] S. K. Chan, S. Em, Sensitivity Analysis, A, Ed, Wiley Series in Probability and Statistics, 2000.

[42] K. ’Stefan, N. ’Ursula, K. ’Pedro, M. ’Edward, What can we learn from global sensitivity analysis of biochemical systems? PLoS One 8 (11) (2013).

[43] I.M. Soboĺ, Sensitivity estimates for nonlinear mathematical models, Math. Model. Comput. Exp. 1 (1993) 407–414.

[44] A. ’, ’Tarantola, S., & ’Chan, K.P.S. ’ ’Saltelli, "A quantitative model-independent method for global sensitivity analysis of model output," vol. 41, no. 1, pp. 39–56, 1999.

[45] A. Paola, I. Azzini, F. Campolongo, M. Ratto, S. Tarantola, A. Saltelli, Variance based sensitivity analysis of model output. Design and estimator for the total sensitivity index, Comput. Phys. Commun. 181 (2010) 259–270.

[46] P.J. Milner, J.D. Martell, R.L. Siegelman, D. Gygi, S.C. Weston, J.R. Long, Overcoming double-step CO2 adsorption and minimizing water co-adsorption in bulky diamine-appended variants of Mg2(dobpdc), Chem. Sci. 9 (1) (2017) 160–174, https://doi.org/10.1039/c7sc04266c.

[47] F. ’Olga, E. ’Christian, B. ’Mahdi, Techno-economic assessment of CO2 direct air capture plants, J. Clean. Prod. 224 (2019) 957–980.

[48] S. ’Bardow, A. ’Deutz, Life-cycle assessment of an industrial direct air capture process based on temperature–vacuum swing adsorption, Nat. Energy 6 (2021) 203–213.

[49] Latitude media, "Carbon removal's tricky transition to early commercialization," https://www.latitudemedia.com/news/carbon-removals-tricky-transition-to-early-commercialization/.

[50] Friedel Pretorius, "Carbon dioxide removal by direct air capture," https://climeworks.com/uploads/documents/direct-air-capture-methodology_climeworks_2022-1692890675.pdf.

[51] A. Sinha, L.A. Darunte, C.W. Jones, M.J. Realff, Y. Kawajiri, Systems design and economic analysis of direct air capture of CO2 through temperature vacuum swing adsorption using MIL-101(Cr)-PEI-800 and mmen-Mg2(dobpdc) MOF adsorbents, Ind. Eng. Chem. Res. 56 (3) (2017) 750–764, https://doi.org/10.1021/acs.iecr.6b03887.

[52] B.M. Balasubramaniam, P.T. Thierry, S. Lethier, V. Pugnet, P. Llewellyn, A. Rajendran, Process-performance of solid sorbents for direct air capture (DAC) of CO2 in optimized temperature-vacuum swing adsorption (TVSA) cycles, Chem. Eng. J. 485 (2024) 149568, https://doi.org/10.1016/J.CEJ.2024.149568.

[53] F. Sabatino, A. Grimm, F. Gallucci, M. van Sint Annaland, G.J. Kramer, M. Gazzani, A comparative energy and costs assessment and optimization for direct air capture technologies, Joule 5 (8) (2021) 2047–2076, https://doi.org/10.1016/J.JOULE.2021.05.023.